

Clinopyroxene/melt trace-element-partitioning in sodic alkaline magmas

Charles D. Beard^{a,b,*}, Vincent J. van Hinsberg^b, John Stix^b, Max Wilke^{c,d}

^a*British Geological Survey, The Lyell Centre, Research Avenue South, Edinburgh, EH14 4AP, UK*

^b*Earth and Planetary Sciences, McGill University, 3450 University Street, Montreal, Québec, H3A 0E8, Canada*

^c*Institut für Erd- und Umweltwissenschaften, Universität Potsdam, Golm, Germany*

^d*Chemie und Physik der Geomaterialien, Deutsches GeoForschungsZentrum GFZ, Potsdam, Germany*

Abstract

Clinopyroxene is a key fractionating phase in alkaline magmatic systems, but its impact on metal-enrichment processes, and the formation of REE + HFSE mineralisation in particular, are not well understood. To constrain the control of clinopyroxene on REE + HFSE behaviour in sodic (per)alkaline magmas, a series of internally heated pressure vessel experiments was performed to determine clinopyroxene-melt element-partitioning systematics. Synthetic tephriphonolite to phonolite compositions were run H_2O -saturated at 650–825°C with oxygen fugacity buffered to $\log f\text{O}_2 \approx \Delta\text{QFM} + 1$ or $\log f\text{O}_2 \approx \Delta\text{QFM} + 5$. Clinopyroxene-glass pairs from basanitic to phonolitic fall deposits from Tenerife, Canary Islands, were also measured to complement our experimentally derived data set.

The REE partition coefficients are 0.3–53, typically 2–6, with minima

*corresponding author

Email address: cbeard@bgs.ac.uk (Charles D. Beard)

for high-aegirine clinopyroxene. Diopside-rich clinopyroxene (Ae_{5-25}) prefer the MREE and have high REE partition coefficients (D_{Eu} up to 53, D_{Sm} up to 47). As clinopyroxene become more Na- and less Ca-rich (Ae_{25-50}), REE incorporation becomes less favourable, and both the $^{VI}M1$ and $^{VIII}M2$ sites expand (to 0.79 Å and 1.12 Å), increasing D_{LREE}/D_{MREE} . Above Ae_{50} , both M sites shrink slightly and HREE ($^{VI}r_i \leq 0.9$ Å \approx Y) partition strongly onto the $^{VI}M1$ site, consistent with a reduced charge penalty for $\text{REE} \leftrightarrow \text{Fe}^{3+}$ substitution.

Our data, complemented with an extensive literature database, constrain a model that predicts trace-element-partition coefficients between clinopyroxene and silicate melt using only mineral major-element compositions, temperature and pressure as input. The model is calibrated for use over a wide compositional range and can be used to interrogate clinopyroxene from a variety of natural systems to determine the trace-element concentrations in their source melts, or to forward model the trace-element evolution of tholeiitic mafic to evolved peralkaline magmatic systems.

Keywords: rare earth elements, aegirine, experimental petrology, Canary Islands, phonolite, peralkaline

1. Introduction

Sodic clinopyroxene appear to more readily incorporate REE than their calcic equivalents (Marks et al., 2004), but despite fractionation of these minerals, melts in evolved alkaline systems can attain high REE contents, even up to economic levels (Kogarko, 1990; Downes et al., 2005; Marks et al., 2011; Sjöqvist et al., 2013; Goodenough et al., 2016; Möller and Williams-Jones, 2016). Trace-element data may be used to model magmatic processes (Spera and Bohrson, 2001; Troll and Schmincke, 2002; Boudreau, 2004; Xu et al., 2010; Girnis et al., 2013; Mungall and Brenan, 2014), but their interpretation requires precise knowledge of mineral/liquid element-partition coefficients. The approach has been applied to studies of mafic systems and mantle melting processes (Niu, 2004; Workman and Hart, 2005; Foley et al., 2013; Coumans et al., 2016; Peters et al., 2017). However, poor constraints on element-partitioning behaviour in alkaline and peralkaline rocks thus far preclude widespread application in these systems.

Experimental investigations of element-partitioning behaviour in alkali-enriched systems are limited in terms of composition (Wood and Trigila, 2001; Huang et al., 2006), and none yet have explored peralkaline conditions where molar $(\text{Na}+\text{K})/\text{Al}$ exceeds 1. Additional information has been obtained from natural samples by measuring the concentration ratios of phenocryst–glass pairs from volcanic and intrusive rocks (Larsen, 1979; Wörner et al., 1983; Shearer and Larsen, 1994; Severs et al., 2009; Fedele et al., 2009; Mollo et al., 2016). However, these results may be biased by the presence of melt inclusions, mineral inclusions and mineral zoning, and their interpretation is commonly complicated by unknown or poorly constrained P-T-H₂O-*f*O₂ con-

²⁶ ditions of equilibration and assumptions of closed-system behaviour.

²⁷ In this contribution, we present trace-element-partition coefficients be-
²⁸ tween sodic clinopyroxene and silicate melts of tephriphonolite to phonolite
²⁹ composition, as determined from internally heated pressure vessel experi-
³⁰ ments on synthetic and natural compositions. These are complemented by
³¹ well-constrained natural volcanic phenocryst-glass pairs from Canary Islands
³² pyroclastic fall deposits. We characterise the mineral compositional controls
³³ on element-partitioning behaviour and present a predictive model for clinopy-
³⁴ roxene/melt element-partitioning that can be used to generate clinopyrox-
³⁵ ene/melt partition coefficients using only clinopyroxene major-element com-
³⁶ positions (e.g., as measured by electron-microprobe). This approach permits
³⁷ forward modelling of element budgets during differentiation processes in mag-
³⁸ matic systems, including evolved sodic alkaline systems, as well as providing
³⁹ a mineral-based tool that can be used to reconstruct parental melt composi-
⁴⁰ tions from clinopyroxene compositions in natural rocks.

⁴¹ 2. Methodology

⁴² 2.1. Experiment starting materials

⁴³ Clinopyroxene were synthesised in sodic alkaline silicate melts of varying
⁴⁴ composition to obtain a range of mineral compositions consistent with those
⁴⁵ in natural systems. Starting glass compositions are given in Table 1 and Fig-
⁴⁶ ure S1. Synthetic glasses L1 and L5 were prepared from reagent-grade oxide
⁴⁷ and carbonate powders, ground together in an agate mortar, decarbonated
⁴⁸ for 6 hrs at 450°C, then homogenised in air for 3 hrs at 1400°C in a Pt cru-
⁴⁹ cible. Repeated fusion and grinding in agate ensured chemical homogeneity

50 of the starting glasses, which was confirmed by electron-microprobe analyses
51 of the final fused glass. Finely-ground Mud Tank zircon was added to the
52 homogeneous major-element glasses as a source of Zr, Hf, Nb and Ta; the
53 glasses were then fused for a further three hours at 1400°C. The remaining
54 trace-elements were added as a cocktail of single-element nitrate solutions
55 (ICP-MS standards), dried onto the powdered glasses, then denitrified at
56 450°C for 30 minutes. The synthetic basanite L1 and phonolite L5 were
57 mixed in varying proportions to make the low alkali (L) series of starting
58 glasses, while dried NaOH and KOH powders were added to make the mid-
59 dle (M) and high (H) alkali starting glasses. Analyses of glass compositions
60 L5 and H5, quenched from superliquidus conditions, confirm that Henry's
61 law was respected (Appendix A).

62 A well-mixed rock powder from the Nechalacho Layered Suite in Canada
63 (Möller and Williams-Jones, 2016, Unit NLS-9, sample L09-194-405.5, al-
64 ternative sample name VM 11-6) was used as experimental starting mate-
65 rial for a more extreme peralkaline composition. This composition was not
66 fused prior to loading into experiment capsules, so as to preserve the origi-
67 nal volatile-element concentrations. An experiment using this material that
68 was quenched from superliquidus conditions is homogeneous with respect to
69 major-elements, as determined from electron-microprobe measurements.

70 *2.2. Experimental equipment and procedures*

71 In total, 36 partitioning experiments were conducted in a Harwood-type
72 internally heated pressure vessel (IHPV) in the HP-GeoMatS laboratory at
73 the German GeoForschungsZentrum (Appendix A). Temperature was mea-
74 sured with Type-S thermocouples calibrated against the melting point of

⁷⁵ NaCl (Borchert et al., 2010, accuracy of ± 5 °C at 200 MPa). Argon gas
⁷⁶ was used as the pressure medium, and pressure was measured with a strain
⁷⁷ gauge to an accuracy of ± 7 MPa. During the experiments, pressure was
⁷⁸ controlled automatically and held within ± 5 MPa of stated values.

⁷⁹ Oxygen fugacity was buffered to the intrinsic redox conditions of the
⁸⁰ experimental setup, which corresponds to $\log f\text{O}_2 \text{ ca. } \Delta\text{QFM} + 1$ in our H₂O-
⁸¹ saturated charges (see Chou, 1986; Berndt et al., 2002; Jugo et al., 2010). One
⁸² experiment using the Nechalacho Layered Suite composition was performed
⁸³ in a double capsule with a haematite solid buffer, designed to increase $f\text{O}_2$
⁸⁴ and promote crystallisation of Fe³⁺-rich clinopyroxene (Eugster and Wones,
⁸⁵ 1962). This experiment ran at the Hm-Mt buffer, which corresponds to
⁸⁶ $\log f\text{O}_2 \approx \Delta\text{QFM} + 5$, as confirmed by presence of both buffer minerals in
⁸⁷ the outer capsule following quench. The experiments were designed to run
⁸⁸ between the liquidus and solidus for each composition, which corresponds to
⁸⁹ temperatures between 650 and 825°C, all at 200 MPa pressure (Appendix
⁹⁰ A).

⁹¹ Powdered starting glass and distilled, deionised water were welded inside
⁹² 3.0 or 3.5 mm outer diameter platinum capsules of 20–25 mm length (see
⁹³ Appendix A). To verify that capsules were sealed, they were heated to 110°C
⁹⁴ and weighed before and after run. The amount of water sealed inside the
⁹⁵ capsules varied with temperature and composition and was kept in excess
⁹⁶ of saturation (Carroll and Blank, 1997; Moore et al., 1998; Schmidt and
⁹⁷ Behrens, 2008). Water saturation was confirmed post-run by puncturing
⁹⁸ capsules and checking for water expulsion and mass loss on drying at 110°C.

⁹⁹ The capsules were loaded into the vessel, pressurised to 200 MPa, then

100 heated to superliquidus temperatures for at least 16 hrs (Appendix A) to
101 permit homogenisation of trace-element concentrations, dissolution of water
102 and equilibration of $f\text{O}_2$ by exchange of H_2 through the capsule wall (cf.
103 Gaillard et al., 2002). Following homogenisation, temperature was lowered
104 to run conditions. An initial set of experiments were cooled rapidly from
105 homogenisation to run temperature at about 100°C/min. A second set of
106 experiments were cooled to run temperature at 1°C/min to promote slow
107 growth of crystals and to minimise the formation of compositional gradients
108 in the melt. Vessel temperature was then cycled between run temperature
109 and run temperature + 10°C to promote dissolution of small crystals at the
110 expense of larger grains, and to promote crystal growth close to the run
111 temperature. Element partitioning results are consistent among experiments
112 of different cooling paths. In all experiments, run temperature was kept
113 constant for at least 40 hrs to allow for chemical homogenisation of melt and
114 growth of crystals via Ostwald ripening. Capsules were then quenched to
115 room temperature.

116 To minimise the growth of groundmass crystals on cooling, a rapid-quench
117 apparatus was used where possible (Table 2). We have not measured quench
118 rates in this vessel, but the capsules probably cooled at rates of several hun-
119 dred degrees Celcius per second (e.g. Berndt et al., 2002). For the rest of
120 the experiments, quenching was achieved by cutting power to the furnace,
121 which resulted in cooling to below the glass-transition temperature (< 350°C;
122 Giordano et al., 2005) in less than 150 seconds.

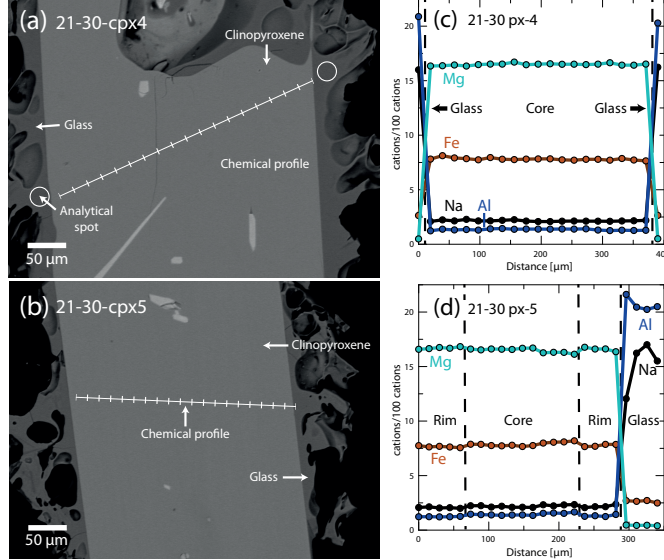


Figure 1: Examples of textural features from Canary Islands clinopyroxene phenocrysts from this study. (a, b) Backscattered electron images show that crystals are euhedral and are free from complex zoning patterns. (c, d) Chemical profiles across clinopyroxene phenocrysts and glass rims (quenched melt), as measured by wavelength dispersive spectroscopy, showing that zoning is effectively absent in these clinopyroxene. In (c) analyses of glass are aligned with the chemical profile shown in (a). Glass analyses shown in (d) are from rims of quenched melt from other clinopyroxene phenocrysts recovered from the same pumice sample. Both pictured phenocrysts are from the basal air fall deposit, associated with the ~2 ka eruption of Pico Viejo, Tenerife (Ablay et al., 1995).

123 *2.3. Natural samples*

124 Alkaline volcanism on Tenerife is associated with a weak thermal mantle
 125 plume that impinges upon thick, old, slow-moving oceanic lithosphere (Car-
 126 racedo et al., 2007). This geological scenario has favoured development of a
 127 complex magma-plumbing system that produces a great diversity of volcanic

¹²⁸ products from alkali basalt to phonolite in composition. The Las Cañadas
¹²⁹ edifice, a large, central, composite stratovolcano (Bryan et al., 1998; Brown
¹³⁰ et al., 2003; Edgar et al., 2007), rests upon a base of at least three mafic al-
¹³¹kaline shield volcanoes (Thirlwall et al., 2000; Guillou et al., 2004; Gurenko
¹³²et al., 2006). Xenoliths indicate that a nepheline syenite intrusive system
¹³³underlies the island (Wiesmaier et al., 2012).

¹³⁴ Six clinopyroxene/glass pairs from four different volcanic eruptions on
¹³⁵Tenerife have been investigated. The ~ 2 ka eruptive products of Montaña
¹³⁶Blanca and Pico Viejo (Ablay et al., 1995) are phonolitic, plinian fall de-
¹³⁷posits, whereas Montaña Samara is a monogenetic, mafic cinder cone (Albert
¹³⁸et al., 2015). Phase-equilibrium experiments conducted on Montaña Blanca
¹³⁹unit UMB-II suggest that magma was stored prior to eruption at $850 \pm 15^\circ\text{C}$,
¹⁴⁰ 50 ± 20 MPa, with 2.5 ± 0.5 wt% H₂O at $\log f\text{O}_2 \approx \text{NNO} - 0.5$ (Andújar and
¹⁴¹Scailet, 2012). Field locations, mineral proportions and major-element com-
¹⁴²positions of the clinopyroxene and glasses are presented in Appendix A.

¹⁴³ 2.4. Sample preparation

¹⁴⁴ Experiment capsules were torn open with pliers, and charges were split
¹⁴⁵using a low-speed wafering saw. Samples were mounted in epoxy resin and
¹⁴⁶polished for *in-situ* chemical analyses.

¹⁴⁷ Natural pyroclastic rocks were rinsed in tap water and crushed with a
¹⁴⁸hammer. Crystals and glass fragments, hand-picked from a sieved size-
¹⁴⁹fraction between 1.18 mm and 125 μm , were used to make grain mounts
¹⁵⁰containing 5–20 crystals of clinopyroxene per sample. Natural samples also
¹⁵¹contain biotite, sanidine, \pm spinel, amphibole, olivine, titanite and sodalite.
¹⁵² Clinopyroxene mineral mounts were examined using backscattered electron

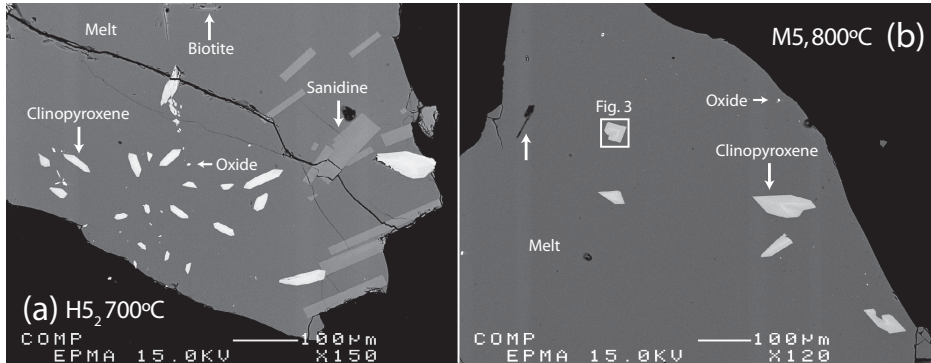


Figure 2: Backscattered electron images showing typical textures of run products from the internally heated pressure vessel experiments. Crystal fractions are typically small (<10% by area), with blade-shaped, euhedral clinopyroxene and glasses free of quench crystals.

153 imaging to select euhedral crystals that were free from melt inclusions and
 154 chemical zoning ($n = 6$, Fig. 1).

155 3. Analytical techniques

156 All experimental products were examined by reflected-light optical mi-
 157 croscopy and scanning electron microscopy, and all phases produced were
 158 identified by electron-microprobe using an energy-dispersive detector. Im-
 159 ages were obtained to estimate modal proportions of phases, which were
 160 calculated using ImageJ freeware (Rasband, 2016, see Appendix A).

161 3.1. Electron-microprobe analysis

162 Major-element compositions of experimental products and natural min-
 163 erals and glasses were measured with a JEOL 8900 instrument at McGill
 164 University and a JEOL 8230 instrument at the University of Ottawa (Table
 165 3). An accelerating voltage of 15 kV was used with a 15 nA beam of $5 \mu\text{m}$

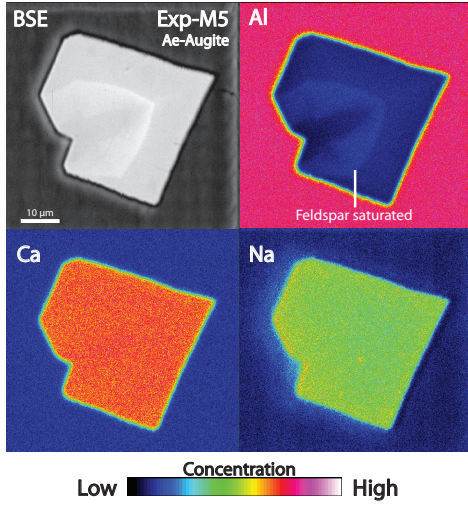


Figure 3: Element maps of clinopyroxene from internally heated pressure vessel experiment M5 (see box in lower magnification image, Fig. 2b). Aegirine-augite clinopyroxene have a sharp internal boundary that reflects feldspar saturation and are subtly zoned. Further element maps are available as an electronic supplement (Fig. S3).

166 diameter for minerals, and a 4 nA beam of $50 \mu\text{m}$ diameter for glasses. Count
 167 times for all elements were 60 sec. Using the above routine, we observed no
 168 sodium loss over the measurement time period. For the silicate minerals and
 169 glasses, both synthetic and natural minerals or oxides were used for calibra-
 170 tion (see Appendix A). Analytical uncertainties were determined by multiple
 171 analyses of reference materials and duplicate analyses of samples.

172 Element distribution maps were generated with a JEOL 8900 instrument
 173 at McGill University using an accelerating voltage of 15 kV, a focussed 40
 174 nA beam, and a dwell time of 50 ms per pixel (Figs. 3, S3). Fe, Ti, Al, Si
 175 and Na were measured with wavelength-dispersive detectors, while Ca and
 176 Mg were measured with an energy-dispersive spectrometer.

177 Transects of Ce, Mg and Fe concentrations within the experiment clinopy-
178 roxene were measured with a JEOL 8900 instrument at McGill University
179 using a focussed beam of 50 nA with an accelerating voltage of 20 kV. Ce was
180 counted with a wavelength-dispersive spectrometer with an LIFH crystal for
181 100 sec (MAC-Ce standard). Mg and Fe were counted for 20 sec, with TAP
182 and LIF crystals respectively (diopside and olivine standards, respectively).
183 Matrix corrections for Mg, Fe and Ce were not possible with these data, for
184 lack of other major-elements measured, however their relative values may
185 still be used to assess the extent to which the clinopyroxene are chemically
186 zoned.

187 *3.2. Laser-ablation ICP-MS*

188 Trace-element concentrations of clinopyroxene and glasses were deter-
189 mined by laser-ablation ICP mass-spectrometry. Analyses were performed
190 at McGill University using a NewWave 213 nm Nd-YAG laser system coupled
191 to a Thermo Finnigan iCAP-Qc quadrupole ICP-MS instrument. Typical flu-
192 ence was 3–12 J/cm² (from 80 µm to 8 µm spot sizes), with a repetition rate
193 of 10 Hz. Ablated material was transferred to the ICP-MS in a He flow of 800
194 mL/min and mixed with Ar prior to injection into the plasma. Instrumental
195 drift was monitored by repeat analyses of the primary standard glass BCR-
196 2G, with bias monitored by repeat analyses of secondary standards UTR-2
197 peralkaline rhyolite and USGS-RGM-1 rhyolite glasses (Appendix A). Sam-
198 ple surfaces were pre-ablated to remove residues from polishing materials and
199 to improve ablation efficiency.

200 Primary and secondary standards and an unzoned Canary Islands clinopy-
201 roxene were analysed with beam sizes of 8–80 µm to monitor crater-size-

dependent element-fractionation effects; none were found for the elements reported here. For minerals and glasses in the experimental charges, beam sizes of 8–40 μm and 16–80 μm were used, respectively. Depending on grain-size and availability, 5–14 mineral grains and 3–10 areas of glass were analysed per charge. Natural clinopyroxene and rim glasses were analysed using a beam size of 12–80 μm and 12–30 μm , respectively. Wherever possible, ablation was performed along lines parallel to crystal rims (1–3 $\mu\text{m} / \text{sec}$).

Drift corrections and data reduction were conducted in Iolite v2.5 (Paton et al., 2011). The total of major-elements measured by LA-ICP-MS or, where available, the Al concentration from electron-microprobe analyses, was used as an internal standard (Table 3). For some experiments, ablation through the minerals was too rapid to generate a stable signal for data-reduction purposes. In these cases, a mixing model was applied to estimate the composition of these clinopyroxene, similar to those applied by Rubatto and Hermann (2007); Yang et al. (2018, and see our Appendix C).

4. Results

4.1. Run product phase stability and crystallinity

Trace-element partition-coefficients are reported for eleven experimental charges. 25 additional experiments were rejected as their run temperatures were superliquidus or subsolidus, or because their growth textures were indicative of disequilibrium (e.g. Fig. S3). Phase proportions are provided in Appendix A.

All reported experimental runs were near-liquidus (3–22% crystals, RL images) and are characterised by a homogeneous distribution of phases (Fig

226 2), except for experiments H5₃ and NLS-9_{2-HM}, in which sanidine crystals
227 are concentrated at the centre. Glasses are clean, homogeneous and show a
228 limited range of major- and trace-element compositions for each experiment
229 (Fig. S1). Clinopyroxene crystals are generally small, euhedral blades with
230 a narrow range of sizes for a given experiment (<10 µm to 100 µm in cross
231 section, Figs. 2–3). In addition to clinopyroxene and glass, experiments on
232 mafic to intermediate compositions produced magnetite, titanite ± kaersu-
233 tite amphibole, whereas some phonolitic experiments produced biotite, alkali
234 feldspar ± magnetite (Appendix A).

235 Constraining the full phase equilibria of all of the investigated composi-
236 tions was beyond the scope of this study. However, in our experiments it
237 can be seen that clinopyroxene has a wide stability field across the inves-
238 tigated physicochemical conditions with only a single starting composition
239 generating amphibole in place of pyroxene (experiments L3 and L3₂). Run
240 conditions and run products given in Appendix A.

241 *4.2. Glass compositions*

242 All run-product glasses are homogeneous across the length and breadth
243 of the experiment capsules based on multiple electron-microprobe and laser-
244 ablation ICP-MS analyses. Most major-element oxide compositions, as mea-
245 sured by electron-microprobe, show relative standard deviations of < 5%
246 within experiment capsules, with minor-elements oxides (concentration <
247 1%) showing greater variability, most with standard deviations between 5
248 and 10 % relative. Trace-element-compositions of the glass, as measured by
249 laser-ablation ICP-MS, typically show time-weighted relative standard de-
250 viations of 1 to 8% within each capsule, with this variability depending on

both the absolute concentration of that element and on the beam-size that was used for analyses (Appendix A). Low sum-totals of major-element oxide concentrations in the electron-microprobe analyses are a result of high dissolved-water contents in the quenched melt.

On a total-alkalies vs. silica diagram the experiment glasses are predominantly phonolitic in composition, though span the trachyte-phonolite join (Fig. S1). Their alkalinity index (molar $(\text{Na} + \text{K})/\text{Al}$) is 0.85 to 1.40, crossing the alkaline–peralkaline join, and the Mg# of these quenched melts is 0 (Mg-free) to 22. The dissolved water content of these quenched melts is 8.8 to 10.7 wt.% (by difference method from EPMA data, with the Fe oxidation state assigned following Kress and Carmichael 1991) and their NBO/T ratios are 0.98 to 1.42 (Mysen et al., 1982, 1985). The halogen content of the synthetic experiments is nominally zero, whereas glasses from the Nechalacho Layered Suite composition experiments typically contain 0.1 % F and 0.02 % Cl by weight.

The Canary Islands glasses are mostly trachytic to phonolitic, with one basaltic trachy-andesite (sample 17-12, Montaña Samara), and are alkaline to weakly peralkaline in composition (A.I. of 0.78 to 1.16) with Mg# of 8 to 39. Dissolved water content and NBO/T ratios are not reported for these glasses because of post-eruptive loss of volatiles. These Canary Islands glasses typically contain 0.2 % F and 0.4 % Cl by weight.

4.3. Compositions of the clinopyroxene and major-element exchange

Experiments on the synthetic compositions produced clinopyroxene of diopside to aegirine-augite composition ($\text{Di}_{29-82}, \text{Ae}_{9-45} \text{ Hd}_{7-33}$), a subset of which overlap with the compositional space defined by the Canary Islands

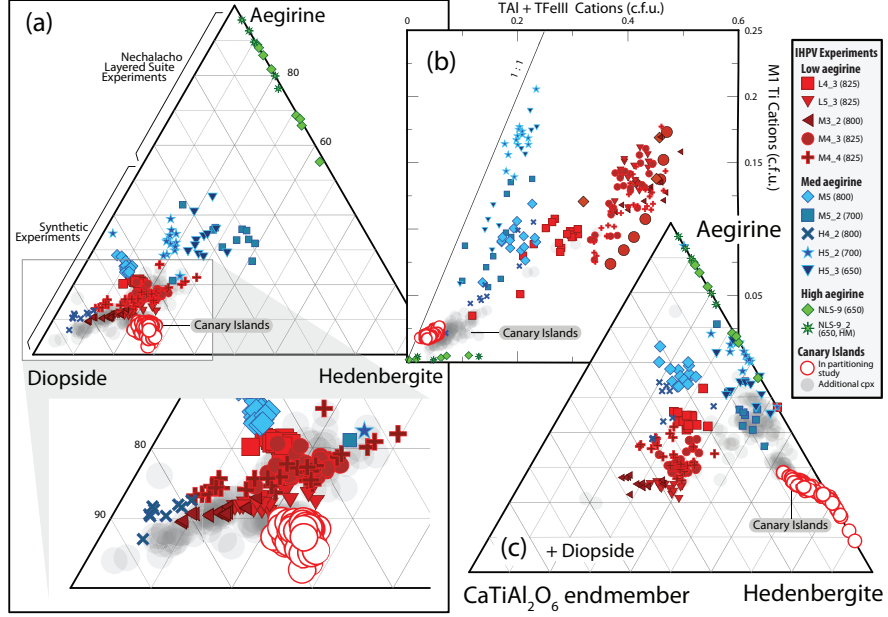


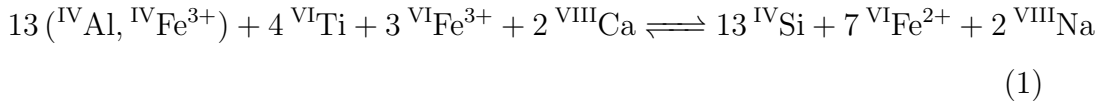
Figure 4: Clinopyroxene grown in internally heated pressure vessel experiments and separated from Canary Islands pyroclasts (a) expressed in terms of diopside, hedenbergite and aegirine end-members, (b) their $V^I_{\text{M1}} \text{Ti}$ and tetrahedral Al and Fe^{3+} contents, and (c) expressed in terms of aegirine, hedenbergite and the theoretical $\text{CaTiAl}_2\text{O}_6$ end-member (Akasaka and Onuma, 1980). $\text{Fe}^{2+}/\text{Fe}^{3+}$ within the clinopyroxene was assigned following Droop (1987), then site occupancies and end-member proportions were allocated following Morimoto (1989). For methods used in calculation of the end-member proportions see Appendix F. The range of clinopyroxene compositions within each experiment records changes to the composition of the melt during crystal growth, whereby the cores of the crystals record the first stage of crystallisation and the rims (highest Fe, Na) are in equilibrium with the quenched melt. Rims of these clinopyroxene are preferentially sampled in trace-element analyses by LA-ICP-MS.

276 clinopyroxene on a diopside–hedenbergite–aegirine ternary diagram (Fig. 4a,
 277 Table 3 and Appendix A). This low-aegirine group of synthetic clinopyrox-

ene display a positive correlation between $^{IV}\text{Al} + ^{IV}\text{Fe}^{3+}$ (in the T-site) and ^{VI}Ti content (in the $^{VI}\text{M1}$ site, red, *low aegirine*, Ae_{5-25} , Fig. 4b), and notably contain both of these elements at elevated concentration relative to the Canary Islands clinopyroxene ($^{IV}\text{Al} + ^{IV}\text{Fe}^{3+} = 0.20\text{--}0.49$ c.f.u., $^{VI}\text{Ti} = 0.07\text{--}0.17$ c.f.u.) . A further subset of synthetic clinopyroxene have higher aegirine content (blue, *med aegirine*, Ae_{25-50}) and show a similar range of Ti content to the low aegirine synthetic minerals (0.05–0.18 c.f.u.), but a limited range of lower $^{IV}\text{Al} + ^{IV}\text{Fe}^{3+}$ content (0.1–0.25 c.f.u., Fig. 4b). Experiments performed on the Nechalacho Layered Suite composition (NLS-9, NLS-9_{2-HM}, green, *high aegirine*, Ae_{55-95}) reproduced the aegirine-augite to aegirine clinopyroxene from the natural system (Möller and Williams-Jones, 2016) that contain low concentrations of $^{IV}\text{Al} + ^{IV}\text{Fe}^{3+}$ (up to 0.14 c.f.u.) and almost no Ti or Mg.

The Canary Islands clinopyroxene that were selected for determination of mineral–melt partition coefficients are diopside in composition (Di_{65-71} , Ae_{3-10} Hd_{21-28}), with most crystals containing about 0.05 c.f.u. $^{IV}\text{Al} + ^{IV}\text{Fe}^{3+}$ and 0.02 c.f.u. ^{VI}Ti (Fig. 4b). These minerals are free from melt inclusions, suggesting slow rates of crystal growth (Kennedy et al., 1993, Fig. 1). Chemical zonation, if present, is of a similar magnitude to the analytical precision of our electron microprobe, indicating that pressure, temperature and melt composition remained stable during crystal growth (Fig. 1). Trace-element abundances within these Canary Islands clinopyroxene show core-to-rim variations of about 1–5 % relative, with larger variations in element abundance associated with sector zoning than with concentric growth zoning (Appendix A).

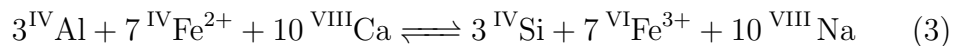
303 By contrast our experiment clinopyroxene display systematic composi-
 304 tional variation between their cores and rims; this variation recording changes
 305 to melt composition during growth of these crystals (e.g. Fig. 3). The sys-
 306 tematics of crystal-chemical zonation both within individual experimental
 307 charges and within groups of experiments reveal major-element exchange
 308 vectors between the clinopyroxene and the melt. Three major-element ex-
 309 change mechanisms correspond to the low (Ae_{5-25}), medium (Ae_{25-50}) and
 310 high (Ae_{55-95}) aegirine compositional domains defined above (Figs. 4b, 5
 311 and S4).



312 For the low-aegirine series,



313 For the medium-aegirine series, and



314 For the high-aegirine series. As the aegirine content of clinopyroxene in-
 315 creases, substitutions at the IVT site become relatively less important than
 316 exchanges at the VIM1 and VIM2 sites (Fig. 5). At the VIM1 site, the im-
 317 portance of Ti substitution for ions of 2+ and 3+ valence also decreases with

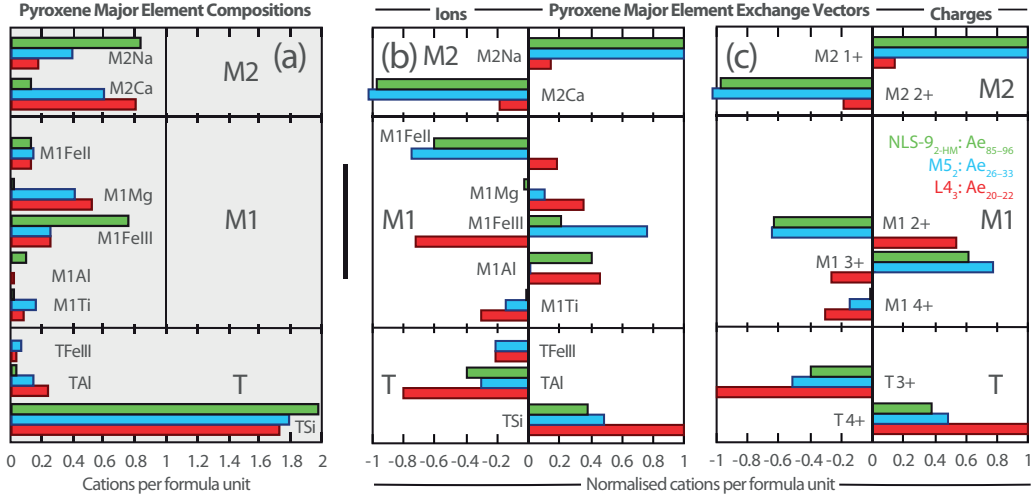


Figure 5: Bar charts showing clinopyroxene composition and major-element exchange mechanisms for three experiments representative of high (green), medium (blue) and low-aegirine (red) clinopyroxene. (a) clinopyroxene major-element compositions are expressed as cations per six-oxygen formula unit (b) exchange mechanisms grouped by ions, (c) grouped by charges. Methods used to calculate these exchange mechanisms are available in the caption of Supplementary Figure S4.

318 increasing aegirine content in the clinopyroxene. In low-aegirine clinopyrox-
 319 ene, the concentration of $3+$ ions at the ${}^{VI}M1$ site is negatively correlated
 320 with X_{Na}^{M2} , whereas in medium- and high-aegirine clinopyroxene, the ${}^{VI}M1$
 321 site takes progressively more $3+$ ions as X_{Na}^{M2} increases. Substitutions of
 322 $VIII\text{Ca}$ for $VIII\text{Na}$ are relatively unimportant in low-aegirine clinopyroxene,
 323 but play a large role in medium- and high-aegirine exchange vectors.

324 **Ends abruptly. add implications for incorporation mechanisms
 325 for trace-elements into clinopyroxene? Or perhaps just refer to the
 326 exchange mechanisms as in melt section below (Putirka, Mollo)?**

327 4.4. Trace-element concentrations in the experiment clinopyroxene

328 Assessing the homogeneity of trace-element-concentrations within min-
329 erals is important when defining mineral–melt partition-coefficients because
330 only the crystal rims record true chemical equilibrium with the adjacent melt.
331 In the case of experimental studies, trace-element analyses of crystal rims are
332 rarely possible because the mineral grains are commonly comparable in scale
333 to the beam-size of laser-ablation or SIMS systems ($\sim 10 - 20 \mu\text{m}$).

334 To quantify the extent to which trace-element-concentrations are zoned
335 within our experiment clinopyroxene, we measured electron-microprobe tran-
336 sects for the elements Mg, Fe and Ce across seven crystals from three ex-
337 periments, each crystallised to varying degrees (Appendix D). These tran-
338 sects reveal that clinopyroxene Ce-concentration follows both sector-zoning
339 and concentric growth-zoning patterns, as recorded by backscattered elec-
340 tron images and the $X\text{Mg}$ of the clinopyroxene. Sector-zoning has a more
341 pronounced effect on the Ce-concentration in the clinopyroxene than concen-
342 tric growth-zoning with bright sectors on BSE images associated with higher
343 Ce-concentrations than dark sectors. To gain insight into the variation of
344 clinopyroxene Ce-concentration associated with concentric growth-zonation,
345 transects across grains were averaged *per-experiment*. Ratios of median aver-
346 age Ce-counts / rim Ce-counts represent the difference between the composi-
347 tion of the bulk crystal, as analysed by LA-ICP-MS, and the composition of
348 the clinopyroxene rims that approach chemical equilibrium with the adjacent
349 quenched melt. For the three experiments measured, bulk/rim Ce ratios are
350 1.04 for M3₂, 1.08 for M5 and 1.12 for M3 1.25F (the latter from Beard,
351 2018).

352 In the case of compatible elements, the analyses of bulk crystal trace-
353 element compositions could therefore return apparent partition coefficients
354 that are overestimated by 4–12% relative to equilibrium values. The highest
355 values are found for the largest clinopyroxene crystals and in these, because
356 of their size, we were able to avoid the cores in the analyses via LA-ICP-
357 MS, thereby reducing the growth-zonation bias in apparent trace-element
358 partition-coefficients.

359 Where large clinopyroxene crystals (ca 100 μm) were present and time-
360 averages of element counts could be used for the reduction of laser-ablation
361 data, trace-element-compositions are similar among clinopyroxene crystals
362 within individual experiments indicating that trace-element concentrations
363 in the melt phase remained spatially homogeneous throughout the duration
364 of the experiments (Appendix A). Typical trace-element concentrations in
365 the experiment clinopyroxene are illustrated in Figure C.6c in Appendix C.

³⁶⁶ **5. Discussion**

³⁶⁷ *5.1. Attainment of equilibrium in the Canary Islands rocks*

³⁶⁸ The Canary Islands trace-element partition-coefficients presented here
³⁶⁹ were determined from euhedral, blade-shaped crystals free of melt inclu-
³⁷⁰ sions and chemical zonation. The corresponding quenched melt was in direct
³⁷¹ contact with these crystals and shows no zonation in backscattered electron
³⁷² images (Fig. 1). While equilibrium conditions are challenging to confirm for
³⁷³ a natural volcanic system, the euhedral forms, chemical homogeneity of crys-
³⁷⁴ tals, and congruency between samples from separate eruptions suggest that
³⁷⁵ the crystals grew in a stable environment, and were not subject to chemical
³⁷⁶ or physical perturbations during growth (Fig. 6). In the case of these Ca-
³⁷⁷ nary Islands clinopyroxene, the entire mineral is interpreted to be in chemical
³⁷⁸ equilibrium with the adhered quenched melt.

³⁷⁹ *5.2. Chemical heterogeneity and approach toward equilibrium during the ex-
periments*

³⁸¹ During our experiments crystals of clinopyroxene were grown directly
³⁸² from unseeded glasses and the run temperature was approached from su-
³⁸³ perliquidus. No attempts were made to reverse these experiments by re-
³⁸⁴ equilibrating crystals and liquids with deliberately mismatched trace-element
³⁸⁵ concentrations because of sluggish diffusion of most elements through the
³⁸⁶ clinopyroxene structure (Van Orman et al., 2001; Cherniak and Dimanov,
³⁸⁷ 2010). As a result of this slow diffusion, all experimental clinopyroxene pre-
³⁸⁸ serve subtle concentric growth-zonation, generated as the cores of the grains
³⁸⁹ become chemically isolated from the melt during growth (see Fig. 4 and Ap-

390 pendix G). Within our clinopyroxene some sector-zonation is also observed,
391 otherwise the major- and trace-element concentrations are generally uniform
392 in the quenched melt and mineral phases (Appendix A).

393 We quantify the departure of apparent partition coefficients from equilib-
394 rium rim compositions with Ce-transects measured across some experiment
395 clinopyroxene via EPMA, with Ce as a proxy for the other compatible el-
396 ements (Appendix D). Concentric growth-zoning has a smaller effect on
397 clinopyroxene Ce-concentration than sector zoning, the former of which was
398 isolated by averaging transects across several grains per experiment. Appar-
399 ent clinopyroxene–melt partition coefficients for compatible elements (median
400 Ce) are offset from equilibrium (rim Ce) to higher values by 4–8% (Appendix
401 D). This systematic positive bias is small relative to the variation in apparent
402 partition coefficients within our sample set, as well as within literature val-
403 ues (e.g. Fig. 7) and shows no correlation with the degree of crystallisation
404 (Appendix D). Furthermore, many of our experimentally-derived apparent
405 partition coefficients plot on trends with clinopyroxene major-element com-
406 position that are defined by a set of literature data (Fig. 7 below). Because
407 the potential bias of our apparent partition coefficients is small relative to
408 the variation in equilibrium values no correction factor has been applied to
409 our data presented in the figures below, or in Table 4 and Appendix A.

410 *5.3. Trace-element-partitioning*

411 Apparent trace-element partition-coefficients and their uncertainties were
412 calculated as mass concentration ratios between clinopyroxene and coex-
413 isting glass and are reported in Table 4 and Appendix A. Where trace-
414 element-concentrations in clinopyroxene could be determined using regular

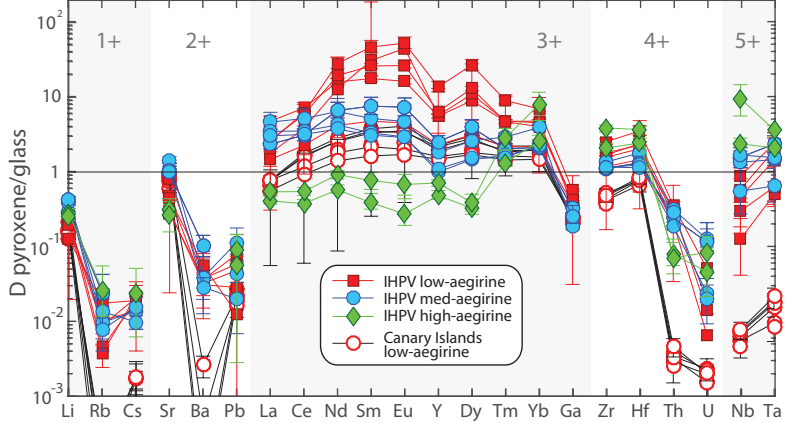


Figure 6: Trace-element partition-coefficients between clinopyroxene and silicate melt, as determined from internally heated pressure vessel experiments ($n = 11$; low-, medium- and high-aegirine types) and from clinopyroxene-rim glass pairs from pyroclastic fall deposits from Tenerife, Canary Islands ($n = 6$; low-aegirine type). Uncertainties on the partition coefficients are at the 1σ level.

time-averages of counts from the ICP-MS system, a time-weighted average composition of clinopyroxene was used with that of the coexisting glass to calculate apparent trace-element partition-coefficients and their associated uncertainty (Appendix A). Where the laser-ablation unmixing model was required for reduction of clinopyroxene trace-element analyses, the partition coefficients were calculated using time-weighted average compositions of glass alongside the corresponding ‘unmixed’ clinopyroxene trace-element concentration (Appendix C). Because a robust-regression data reduction scheme was used, this technique returns a median-average trace-element concentration for clinopyroxene. Derived trace-element partition-coefficients are consistent between these two data-reduction methodologies to better than 2σ . Uncertainty calculations are described in Appendix C.

427 Three markedly different behaviours of rare earth element partitioning are
428 observed in the experiments (Fig. 6). These depend on the aegirine concen-
429 tration in the clinopyroxene and match the major-element exchange vector
430 domains discussed above. Low-aegirine experiment clinopyroxene (Ae_{5-25})
431 prefer the MREE; medium-aegirine clinopyroxene (Ae_{25-50}) show a similar
432 behaviour, save for higher LREE partition coefficients, whereas high-aegirine
433 clinopyroxene (Ae_{55-95}) strongly prefer HREE and show incompatible be-
434 haviour for the light and middle REE. The experiment REE partition co-
435 efficients are 0.3–53, typically 2–6, with minima for LREE and MREE in
436 high-aegirine clinopyroxene (Fig. 6). Apparent REE partition coefficients
437 determined from our experiments are positively correlated with the ^{IV}Al con-
438 tent of the clinopyroxene and are an order of magnitude higher than most
439 literature values, the majority of which were determined for more mafic com-
440 positions (e.g. Fig. 7e). The Canary Islands clinopyroxene show similar
441 rare earth element partitioning systematics to the low-aegirine experiment
442 clinopyroxene, with absolute values for these partition coefficients of about
443 one order of magnitude lower (Fig. 6).

444 The high field-strength elements (HFSE) Zr, Hf, Nb and Ta are compati-
445 ble to slightly incompatible in the experimental clinopyroxene, and typically
446 1–2 orders of magnitude less compatible in the Canary Islands clinopyroxene
447 (Fig. 7a,b,c). D_{HFSE} for the low-aegirine experiments and Canary Islands
448 rocks plot on trends with the ^{IV}Al content of clinopyroxene, as defined by
449 literature data from Italian volcanoes. In our medium- and high-aegirine ex-
450 periments D_{HFSE} values are not correlated with the ^{IV}Al content of clinopy-
451 roxene, consistent with a distinct incorporation mechanism for these ele-

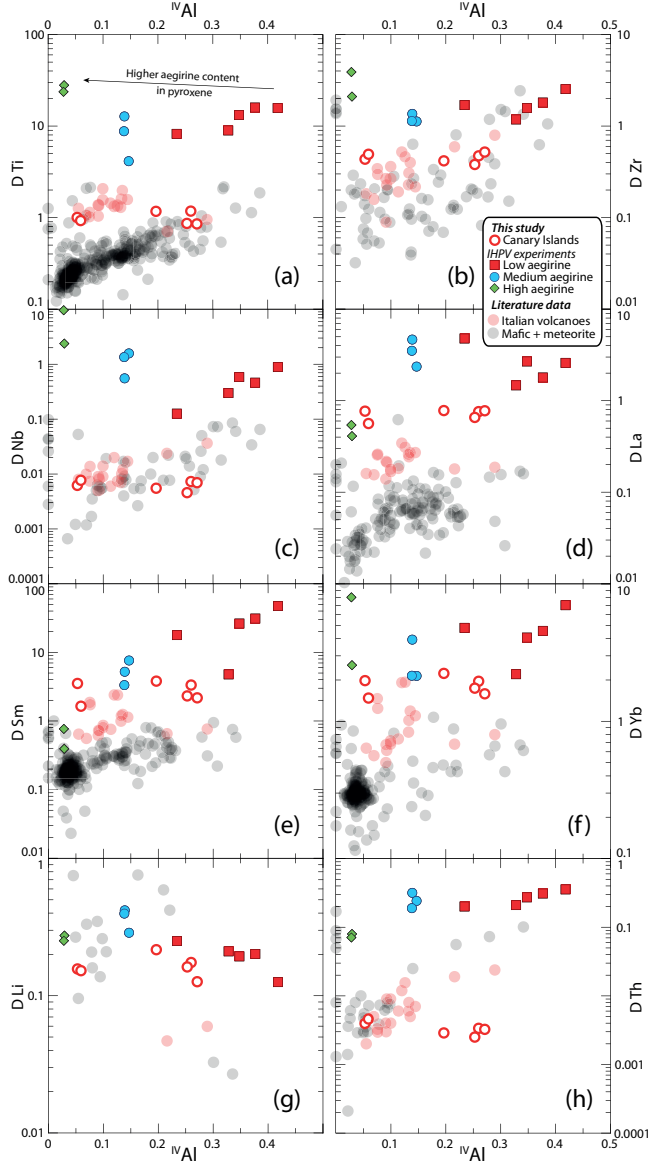


Figure 7: Element partition coefficients for HFSE (Ti, Zr, Nb), REE (La, Sm, Yb) and TE (Li, Th) vs. ^{IV}Al (c.f.u.). Literature values ($n = 411$), including those from potassic Italian volcanoes (red), are from the compilation of Bédard (2014), with additional, more recent, data from Mollo et al. (2016). Figure S5 shows similar diagrams with X_{Na}^{M2} in place of ^{IV}Al .

452 ments relative to the low-aegirine experiments. Partition coefficients for the
453 large-ion lithophile elements K, Sr, Pb are positively correlated with X_{Na}^{M2} in
454 the low- and medium-aegirine clinopyroxene, but are lower in high-aegirine
455 clinopyroxene (Fig. 6, Appendix A). The Rb, Cs and Ba partition coef-
456 ficients have a high uncertainty and are maximum estimates owing to low
457 concentrations of these elements in the clinopyroxene, close to the detection
458 limit for analyses by LA-ICP-MS. Lithium is incompatible ($D_{Li} = 0.1\text{--}0.4$) in
459 both Canary Islands and experimental clinopyroxene and, like Sr and Pb, be-
460 comes more compatible with increasing aegirine content in the clinopyroxene,
461 plateauing at $X_{Na}^{M2} = 0.4$ and decreasing thereafter (Fig. S5g). The actinides
462 U and Th show contrasting partitioning behaviour; the former showing no
463 correlation with aegirine content in the clinopyroxene, the latter becoming
464 more incompatible with increasing aegirine content (Fig. 7h). The U and
465 Th partition coefficients for our Canary Islands samples are similar to those
466 for the Italian volcanoes (Wood and Trigila, 2001; Fedele et al., 2009; Mollo
467 et al., 2013, 2016), and are 1–2 orders of magnitude more incompatible rela-
468 tive to the experimental clinopyroxene.

469 5.4. The effects of melt structure on element-partitioning

470 The partitioning of trace-elements between crystals and melts is con-
471 trolled by their relative activity in each phase and the exchange mechanisms
472 by which their incorporation into crystals takes place (e.g., Jd-melt, Jd-DiHd
473 and CaTS-DiHd exchanges have been shown to control REE incorporation
474 in cpx, Putirka, 2008; Wood and Blundy, 2014; Mollo et al., 2017). In rel-
475 atively polymerised systems ($NBO/T < 0.49$), melt structure can impart a
476 significant influence on partitioning behaviour (Gaetani, 2004; Schmidt et al.,

477 2006; Huang et al., 2006). In our strongly depolymerised peralkaline system
478 apparent partition coefficients are not correlated with NBO/T, except for
479 D_{Sr} that shows a weak positive correlation (Fig. 8). NBO/T could not be
480 calculated for our Canary Islands compositions because the water content of
481 the melt prior to quench is not known.

482 *5.5. Fits to the lattice-strain model*

483 The equilibrium partitioning of trace-elements between minerals and melts
484 is largely controlled by the structure of the crystal lattice, its elasticity (On-
485 uma et al., 1968; Kumazawa, 1969; Weidner and Vaughan, 1982) and its
486 ability to accommodate an excess or shortage in charge (Blundy et al., 1998;
487 Wood and Blundy, 2001; Hanchar et al., 2001; Corgne and Wood, 2005). The
488 lattice-strain model provides a framework in which the influence of these
489 variables on partitioning behaviour can be quantified, and thus predicted
490 under conditions bracketed by a calibrating data set (Onuma et al., 1968;
491 Blundy and Wood, 1994; Wood and Blundy, 2014). The lattice structure of
492 minerals has a dependence on pressure, temperature and composition, and
493 element-partitioning is a thermodynamically-controlled process (e.g. Wood
494 and Blundy, 1997).

495 Most trivalent ions, including the REE and Y enter the M2 site of clinopy-
496 roxene, which is typically 6- or 8-coordinated (Deer et al., 1992). Smaller
497 trivalent ions, including Al, Cr, Ga, Sc, and in the case of Fe-rich clinopy-
498 roxene the HREE may enter the smaller $V^I M_1$ site (Olin and Wolff, 2010;
499 Reguir et al., 2012; Bédard, 2014). The high field-strength elements Ti, Zr,
500 Hf, Nb and Ta are typically hosted by the $V^I M_1$ site (Hill et al., 2000, 2011;
501 Dygert et al., 2014).

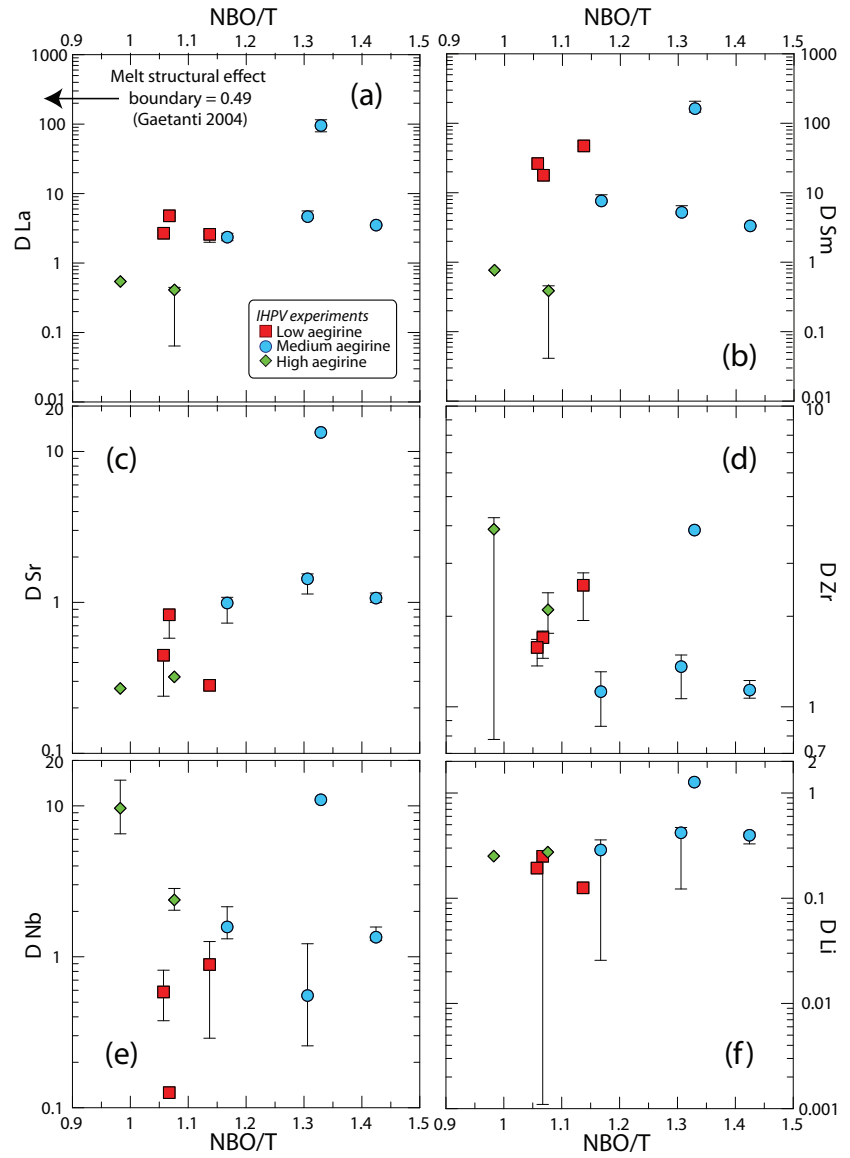


Figure 8: Diagrams of clinopyroxene–melt trace-element partition coefficients for the IHPV experiments as a function of NBO/T of the quenched melt. NBO/T was calculated following Mysen et al. (1985) with melt Fe oxidation state assigned following Kress and Carmichael 1991 and the water content of the melt estimated by difference from 100% major-element oxides.

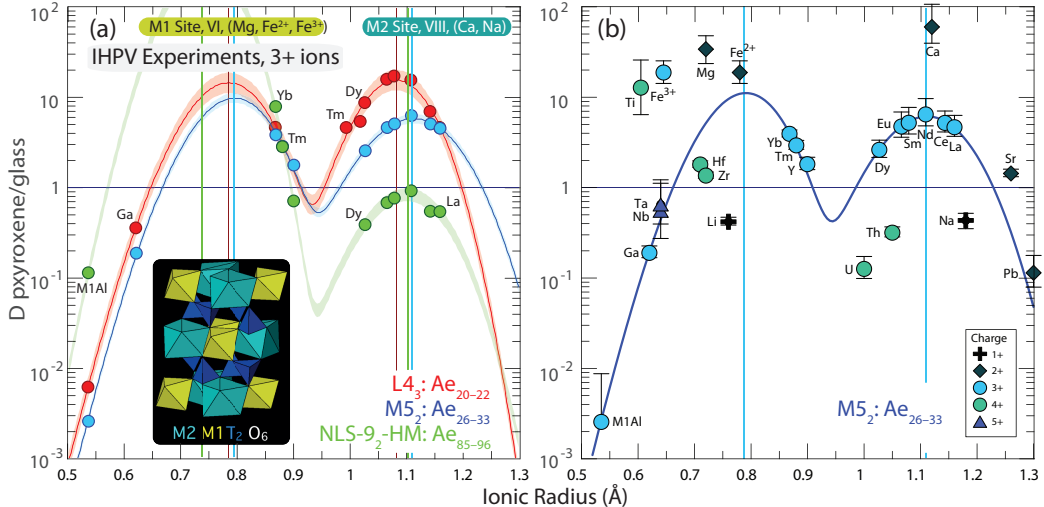


Figure 9: Non-linear weighted least-squares fits to element-partitioning data from the internally heated pressure vessel experiments following the lattice-strain model of Blundy and Wood (1994). (a) Representative fits to 3+ ion partitioning behaviour with examples for low (red), medium (blue) and high-aegirine (green) clinopyroxene experiments. (b) Measured partition coefficients for ions of 1+, 2+, 4+ and 5+ charges that are consistent with the lattice-strain model. Ionic radii are assigned to 6 or 8 fold co-ordination (Shannon, 1976), and were chosen to minimise residuals in the fit (cf. Olin and Wolff, 2010). Y was not included in the fitting routine for 3+ ions because of mass fractionation effects (ibid.). Vertical coloured lines indicate ideal ionic radii (r_0) of ^{VI}M1 and ^{VIII}M2 sites and shaded areas indicate 95% confidence intervals on the fits determined via bootstrapping. Uncertainties on the partition coefficients in (b) are 1σ . Fitted lattice-strain parameters are given in Table 4.

502 To investigate systematics in D_i values and the mechanisms by which
 503 trace-elements are incorporated into clinopyroxene, element-partitioning be-
 504 haviour was explored in light of the lattice-strain theory, quantitatively de-
 505 scribed by the lattice-strain equation:

$$D_i^{mineral/melt} = D_0 \exp \left[\frac{-4\pi E_s N_a}{RT} \left(\frac{r_0}{2} (r_0 - r_i)^2 - \frac{1}{3} (r_0 - r_i)^3 \right) \right] \quad (4)$$

506 where r_0 is the ideal radius for the lattice site, E_s is the Young's modulus (i.e.,
 507 the lattice site stiffness in GPa), D_0 is the strain-free partition coefficient, N_a
 508 is Avagadro's number, R is the gas constant, T is temperature in Kelvin, and
 509 r_i is the ionic radius of the element in question, all radii in Å. We focused on
 510 3+ ions that cover a wide range of radii and fitted lattice-strain parameters
 511 for both the ^{VI}M1 and ^{VIII}M2 sites of clinopyroxene (Fig. 9):

$$D_i^{cpx/melt} = D_0^{M2} \exp \left[\frac{-4\pi E_s^{M2} N_a}{RT} \left(\frac{r_0^{M2}}{2} (r_0^{M2} - r_i)^2 - \frac{1}{3} (r_0^{M2} - r_i)^3 \right) \right] + D_0^{M1} \exp \left[\frac{-4\pi E_s^{M1} N_a}{RT} \left(\frac{r_0^{M1}}{2} (r_0^{M1} - r_i)^2 - \frac{1}{3} (r_0^{M1} - r_i)^3 \right) \right] \quad (5)$$

512 Parabolae for 3+ ions were fitted for the ^{VI}M1 and ^{VIII}M2 sites using the
 513 REE, Ga and Al assigned to the ^{VI}M1 site of clinopyroxene (Fig. 9a). Fits are
 514 weighted based on uncertainties for the element-partition coefficients. HREE
 515 have higher element-partition coefficients than can predicted by substitution
 516 into the ^{VIII}M2 site, hence were fitted with ionic radii for sixfold coordination
 517 into the ^{VI}M1 site (*cf.* Olin and Wolff, 2010; Reguir et al., 2012; Bédard,
 518 2014). Lattice-strain parameters as obtained from fits to the data are shown
 519 in Appendix A.

520 In some low-aegirine experiments and the Canary Islands rocks, lattice-
 521 strain fitting for 3+ ions at the ^{VI}M1 site was not possible, because too few
 522 HREE partitioned onto the ^{VI}M1 site of these clinopyroxene. Here, we chose
 523 to fit only lattice-strain parameters for the ^{VIII}M2 site, or fix D_0^{3+} values for

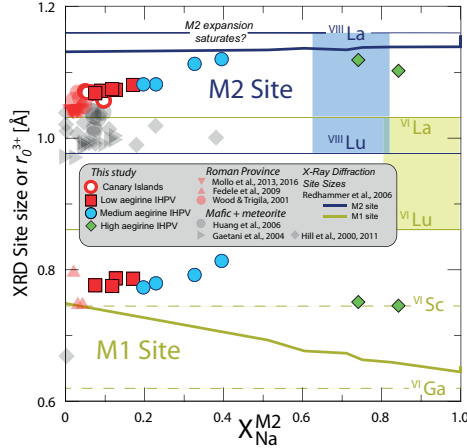


Figure 10: Diagram showing variation of ideal ionic radius r_0^{3+} with $X_{\text{Na}}^{\text{VIII}}\text{M}_2$ for ${}^{\text{VI}}\text{M}_1$ and ${}^{\text{VIII}}\text{M}_2$ sites of clinopyroxene. Shown for comparison are single crystal x-ray diffraction data from the hedenbergite-aegirine compositional join (heavy solid lines, from Redhammer et al., 2006). Shaded boxes represent the range of ionic radii for rare earth elements in VI and VIII coordination (Shannon, 1976). Literature data for Italian volcanoes are from Fedele et al. (2009); Mollo et al. (2013, 2016); Wood and Trigila (2001) and for mafic systems are from Hill et al. (2000, 2011); Gaetani (2004); Huang et al. (2006).

the ${}^{\text{VI}}\text{M}_1$ site to match those for the ${}^{\text{VIII}}\text{M}_2$ site, and fit only the r_0 and E_s parameters for the ${}^{\text{VI}}\text{M}_1$ site (??). Fitting of element-partitioning data for 1+, 2+ and 4+ ions was less successful owing to sparse coverage of suitable radii and detection-limit issues for some elements. Partition coefficients for 1+, 2+, and 4+ elements follow radius- and charge-dependent trends consistent with lattice-strain theory and reported effects of charge on lattice-strain parameters (Fig. 9b, e.g., Hazen and Finger, 1979; Law et al., 2000; Adam and Green, 2006).

532 5.5.1. *Effects of composition on ideal site size, r_0*

533 As the composition of clinopyroxene shifts from augite toward aegirine,
534 the size of the ^{VI}M1 and ^{VIII}M2 sites, or strain-free radii (r_0), should diverge
535 following the sizes of the major-element cations on these sites. Lattice-strain
536 fits for 3+ cations indicate expansion of the ^{VIII}M2 site between low and
537 medium-aegirine clinopyroxene, with r_{0M2}^{3+} correlating well with Na replacing
538 Ca (Figs. 9, 10). Expansion of the ^{VIII}M2 site stalls at $r_{0M2}^{3+}, \approx 1.12 \text{ \AA}$
539 and $X_{Na}^{M2} \approx 0.4$, changing little in size between medium and high-aegirine
540 clinopyroxene. We suggest that this is a ‘saturation effect’, whereby the
541 smaller ions in the ^{IV}T and ^{VI}M1 sites prevent further expansion of the ^{VIII}M2
542 site as additional R_{M2}^+ is added to the clinopyroxene. For the ^{VI}M1 site of
543 clinopyroxene, strain free radii for R^{3+} cations indicate expansion between
544 low and medium-aegirine clinopyroxene and contraction between medium
545 and high-aegirine clinopyroxene (Figs. 9, 10). These trends broadly follow
546 the substitution of Mg^{2+} for Fe^{2+} , then Fe^{2+} for Fe^{3+} with increasing aegirine
547 content in the clinopyroxene.

548 5.5.2. *The effect of cation charge on the D_0 parameter*

549 The D_0 parameter of the lattice-strain model describes ideal, strain-free
550 partitioning and tracks the solubility of an ideal cation in the mineral with
551 changing pressure, temperature and the bulk composition of the system
552 (Wood and Blundy, 2014). D_0 therefore correlates with the major-element
553 composition of the clinopyroxene. Moreover, incorporation of trace-elements
554 of a different charge introduces an electrostatic penalty that leads to a lower
555 D_0 for that charge (Wood and Blundy, 2001, 2003).

556 The average charge of major-elements on the ^{VIII}M2 site of clinopyroxene

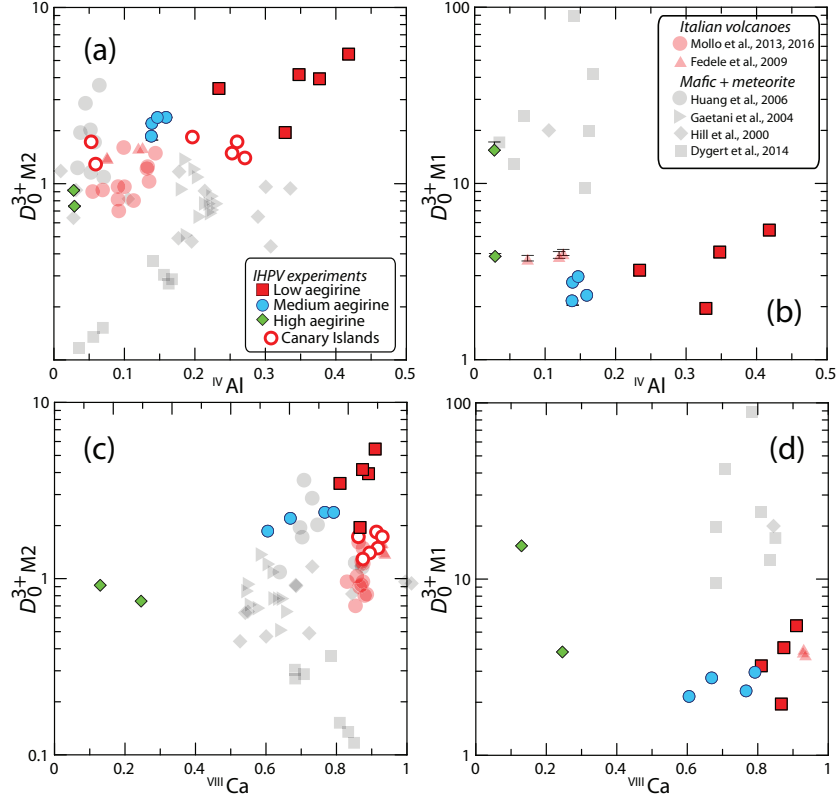


Figure 11: Strain-free partitioning coefficients (D_0) for 3+ ions into clinopyroxene vs. clinopyroxene major-element composition. (a,c) are for the $VIII_{M2}$ site, and (b,d) are for the VI_{M1} site. The diagrams show that variability in partitioning behaviour is highly dependent on mineral composition, and that variation between aegirine-rich clinopyroxene cannot be explained well by the same mechanisms as more mafic systems (c). Literature data for element-partitioning in Mafic + Meteorite and Italian volcano compositions are from the compilation of Bédard (2014). 1σ uncertainties are shown in (a, b) and are usually smaller than the symbol sizes.

decreases from 2+ to 1+ on the compositional join between Ca-rich diopside and Na-rich aegirine. Consequently, the electrostatic penalty for substituting a REE³⁺ cation into the clinopyroxene $VIII_{M2}$ site is increased (Fig. 11e).

560 Conversely, as the average charge on the ^{VI}M1 site of clinopyroxene increases
561 from 2+ toward 3+ in end-member aegirine, the electrostatic penalty in-
562 curred when substituting REE³⁺ cations onto the ^{VI}M1 site is reduced (Fig.
563 11f). $D_{0,M1}^{3+}$ consequently increases by an order of magnitude between our
564 medium-aegirine and high-aegirine experimental clinopyroxene, an effect that
565 when combined with the shrinking ^{VI}M1 site size, leads to strong fractiona-
566 tion of the HREE (Figs. 9 and 11f).

567 A positive correlation between ^{IV}Al and partition coefficients for highly
568 charged trace-elements has been extensively documented in studies on clinopy-
569 roxene (Lundstrom et al., 1994; Gaetani and Grove, 1995; Blundy et al., 1998;
570 Francis and Minarik, 2008; Hill et al., 2011; Mollo et al., 2016). The low-
571 aegirine experimental clinopyroxene and most of the Canary Islands rocks
572 extend trends defined by clinopyroxene from mafic systems (Figs. 7, 11a),
573 whereas the remainder of the experimental data set and Canary Islands rocks
574 show element-partitioning behaviour similar to Italian volcanoes (Wood and
575 Trigila, 2001; Fedele et al., 2009; Mollo et al., 2016), confirming that an ^{IV}Al-
576 controlled substitution mechanism for REE extends to peralkaline conditions
577 (Figs. 7, 11a).

578 D_0^{3+} parameters for the ^{VI}M1 site are strongly correlated with those for
579 the ^{VIII}M2 site, except at aegirine concentrations exceeding 50 mol.%. Sim-
580 ilarities to ^{VIII}M2 partitioning behaviour likely reflect the dominance of T-
581 site substitution mechanisms in augite clinopyroxene. In the high-aegirine
582 clinopyroxene, T-site substitutions become less important as the T-sites be-
583 come saturated with Si⁴⁺ (Fig. 5). The replacement of Fe³⁺ at the ^{VI}M1
584 site by 3+ trace-elements does introduce a charge penalty, therefore $D_{0,M1}^{3+}$

585 increases accordingly.

586 *5.6. An element-partitioning model extending to aegirine clinopyroxene*

587 Partition-coefficients vary systematically with the physicochemical con-
588 ditions of natural and synthetic magmas (cf. Wood and Blundy, 2003). Con-
589 sequently, a host of models have been presented to describe the systematics
590 of element-partitioning between clinopyroxene and silicate melts (Wood and
591 Blundy, 1997, 2001; Hill et al., 2011; Yao et al., 2012; Sun and Liang, 2012;
592 Bédard, 2014; Dygert et al., 2014; Mollo et al., 2016). The majority of these
593 models are based on lattice-strain theory and predict how the lattice param-
594 eters r_0 , E_s , and D_0 vary with composition, temperature and pressure. This
595 semi-thermodynamic approach theoretically permits calculation of partition
596 coefficients for any trace-element, at any set of $P - T - X$ conditions. In re-
597 ality, all models have a limited working range, as restricted by the input data
598 set. Because existing partitioning models do not reproduce the high $r_{0,M2}^{3+}$
599 values for clinopyroxene with aegirine contents ≥ 50 mol % (Fig. 12a), they
600 cannot accurately predict REE partitioning behaviour for strongly peralka-
601 line systems. We therefore present a new empirical model that is calibrated
602 on both our experimental work and natural partition coefficients from Ca-
603 nary Islands rocks ($n = 16$), as well as existing partitioning data from the
604 literature ($n = 75$, compilation of Bédard 2014, and Mollo et al. 2016, Fig.
605 12, Appendix A). Our calibration database covers a wide range of composi-
606 tion, pressure, temperature and oxygen fugacity (0.0001–3.5 GPa, 650–1345
607 °C, $\log f\text{O}_2 = \text{IW to MH} \approx \Delta\text{QFM} -5$ to +5). Clinopyroxene compositions
608 are $X\text{Mg}$ 0.031–1, X_{Na}^{M2} 0–0.84 and ${}^{\text{IV}}\text{Al}$ 0–0.49 c.f.u. and melt composition
609 varies widely in terms of Mg# (0–100) and $X\text{H}_2\text{O}$ (0–0.38). REE parti-

tion coefficients are D_{La} 0.01–4.79; D_{Sm} 0.02–47.24, and D_{Yb} 0.11–8.00. The majority of partition coefficients in the training data set were measured via SIMS or LA-ICP-MS, minimising analytical uncertainty (e.g. from analyses by electron-microprobe).

Our model is based on clinopyroxene composition alone so that it may be applied in geological scenarios where melt composition cannot be directly measured, for example to the cores of zoned phenocrysts in tephra, or to cumulate systems. Partition coefficients between clinopyroxene and melt are controlled by the relative activity of elements in each of these two phases (Wood and Blundy, 2014), therefore an empirical model to predict partition coefficients from both melt and mineral compositional terms has the highest potential for accuracy. Our approach is valid because crystallisation is a thermodynamically-controlled process and the composition of the melt and thus its effects on element-partitioning are, at least in part, recorded by the major-element composition of the clinopyroxene.

5.6.1. The clinopyroxene M2 site

To find the principal physicochemical factors that affect element-partitioning at the ^{VIII}M2 site of clinopyroxene, a stepwise least-squares multiple linear regression analysis was performed using the lattice-strain parameters r_0^{3+} , E_s^{3+} and D_0^{3+} , temperature, pressure and clinopyroxene composition as inputs. Input parameters were initially examined in binary scatter diagrams to ascertain whether correlations with lattice-strain parameters were linear. If not, interaction compositional terms were added to the initial set of possible fitting parameters that had linear correlations with lattice-strain parameters (e.g. $X_{\text{Al}+\text{Fe}^{3+}}^T$). Intensive variables for multiple regression models for r_0 ,

635 E_s and D_0 were introduced following a hierarchical forward selection crite-
 636 rion with switching. The largest number of significant terms to describe a
 637 lattice-strain parameter was eight for E^{M^2} (c.95%, cf. Appendix E).

638 The resultant empirical model accounts well for changes in lattice-strain
 639 parameters over a range of compositions from basalt to peralkaline phono-
 640 lite, faithfully reproducing large $r_0^{M^2}$ values typical for sodic clinopyroxene
 641 (Fig. 12a, model coefficients in Table 5). Student t-tests show that all of
 642 the independent variables included in the models are significant at the 95%
 643 confidence level and PRESS R^2 values obtained by repeated random sub-
 644 sampling of the dataset (Stevens, 1996) are close to R^2 values calculated by
 645 regular methods, indicating that the models are robust and have high pre-
 646 dictive power. Full multiple regression reports are available in Appendix E.
 647 Equations generated by the multiple linear regression calculations are given
 648 below for the ^{VIII}M2 site, where a_i are the regression coefficients for the re-
 649 spective variables:

650

$$\ln D_0^{M^2} = a_1 + a_2 T + a_3 X_{Al+Fe^{3+}}^T + a_4 X_{Ti}^{M^1} + a_5 X_{Al-Fe^{3+}}^{M^1} + a_6 X_{Fe^{2+}}^{M^2} \quad (6)$$

$$E^{M^2} = a_7 + a_8 P + a_9 X_{Al+Fe^{3+}}^T + a_{10} X_{Al}^{M^1} + a_{11} X_{Mg}^{M^1} + a_{12} X_{Ti}^{M^1} \\ + a_{13} X_{Mg}^{M^2} + a_{14} X_{Mg} \quad (7)$$

$$r_0^{M^2} = a_{15} + a_{16} T + a_{17} X_{Al-Fe^{3+}}^{M^1} + a_{18} X_{Ti}^{M^1} + a_{19} X_{Ca}^{M^2} + a_{20} X_{Na}^{M^2} \quad (8)$$

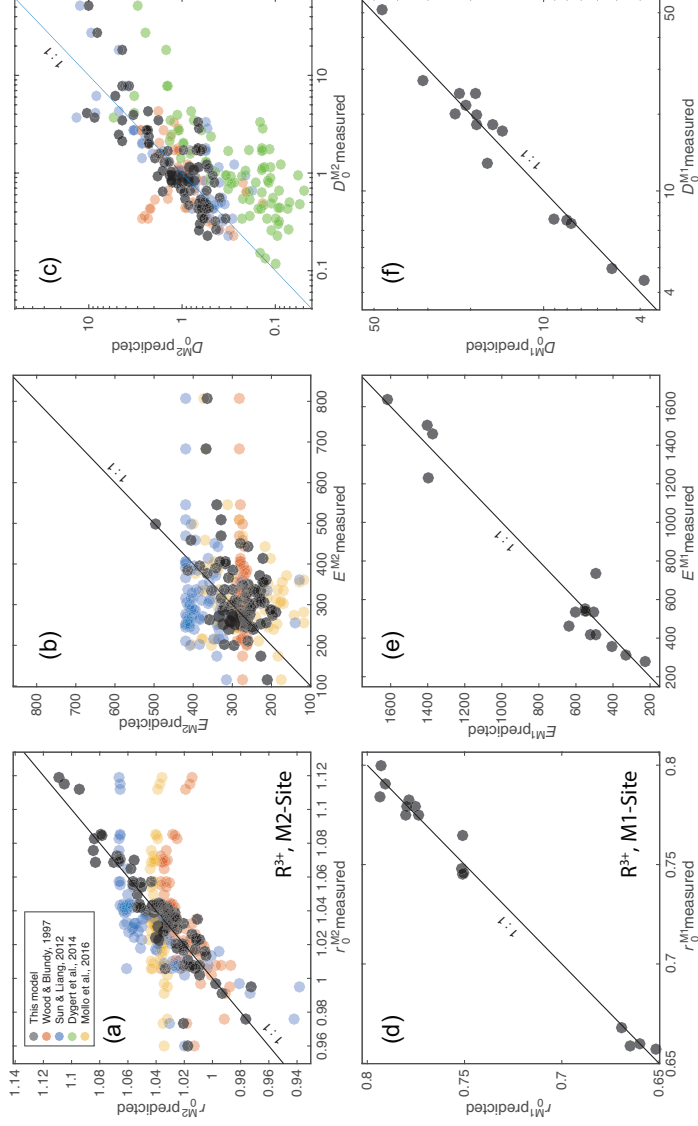


Figure 12: Measured vs. predicted model values for lattice-strain parameters for the $V^{III}M2$ and V^IM1 sites of clinopyroxene. The new models presented here were generated via a stepwise multiple linear regression procedure following a hierarchical forward selection criterion with switching. Full regression reports are in Appendix E and model equations are in the main text.

651 The model for r_0^{M2} is robust with high predictive power and incorporates
652 compositional controls from the ^{VI}M1 and ^{VIII}M2 sites, as well as temper-
653 ature. Elevated concentrations of large ^{VIII}M2 cations Ca^{2+} and Na^+ are
654 correlated with large ^{VIII}M2 sites. Ti^{4+} cations in the neighbouring ^{VI}M1 site
655 are also correlated with expansion of the ^{VIII}M2 site, and the concentration
656 of small Al^{3+} minus larger Fe^{3+} on the ^{VI}M1 site is negatively correlated with
657 r_0^{M2} . The negative correlation between r_0^{M2} and temperature reflects the sum
658 of changes to major-element composition that lead to smaller clinopyroxene
659 ^{VIII}M2 sites at higher temperatures. This compositional effect swamps the
660 minor influence of thermal expansion.

661 The model for D_0^{M2} incorporates compositional terms from all three sites
662 in clinopyroxene and temperature. The positive effect of tetrahedral R^{3+}
663 on D_0^{M2} is the largest contribution to the model, which is consistent with
664 published studies (see above). The relationship between clinopyroxene com-
665 positional terms on the ^{VI}M1 and ^{VIII}M2 sites and D_0 are indirect and are
666 tied to the solubility of the mineral in the melt (Wood and Blundy, 2003),
667 which in turn is tied to the physicochemical conditions of the system (largely
668 melt composition). The model for D_0^{M2} is less robust than that for r_0^{M2} ,
669 largely because there are melt compositional effects that are not recorded
670 in the composition of the clinopyroxene. We tested the Mg# and $X\text{H}_2\text{O}$ of
671 the melt, neither of which are significant predictors for D_0^{M2} (95% confidence
672 interval).

673 The model for E^{M2} is less well-constrained than for the other two ^{VIII}M2
674 lattice-strain parameters, suggesting that ^{VIII}M2 site stiffness is not tied
675 strongly to clinopyroxene composition, temperature or pressure. Despite a

significantly lower predictive power, this model still has physical grounding. Stiffness of the ^{VIII}M2 site is positively correlated with pressure, as might be expected following a simple Hooke's law relationship, and there are some subtle compositional controls imparted by the ^{IV}T and ^{VI}M1 sites. The poor correlation between E^{M2} , clinopyroxene composition, temperature and pressure is also evident in published element-partitioning models, where E^{M2} is either poorly predicted (Fig. 12b), or set to a fixed value (e.g. Dygert et al., 2014).

Diagrams of measured vs. predicted D values for R³⁺ cations are given in Figure 13a, showing the predictive power of the models over a compositional range between basalt and peralkaline phonolite. For the ^{VIII}M2 site, 95% of the measured R³⁺ partition coefficients are reproduced within a factor of ± 2.5 (hard dashed lines), and in extreme cases, the model still reproduces D values within an order of magnitude, sufficient for the prediction of element-partitioning trends over a wide range of $P - T - X$. D_{MREE} , such as Sm, are reproduced more faithfully than D_{LREE} , because their radius is closer to r_0^{M2} (Fig. 13c,d), and therefore prediction of their partitioning behaviour is affected less strongly by inaccuracies in predicted E^{M2} values.

5.6.2. The clinopyroxene M1 site

Using a methodology similar to the ^{VIII}M2 site, we fitted a predictive model for partitioning of R³⁺ cations onto the smaller ^{VI}M1 site of clinopyroxene. Lattice-strain parabola were constrained by partitioning data for Cr, Ga, Sc, and where suitable, the HREE Tm, Yb and Lu (Our IHPV experiments plus Hill et al. 2000; Fedele et al. 2009; Mollo et al. 2013; Dygert et al. 2014). The training data set for the ^{VI}M1 site partitioning model is

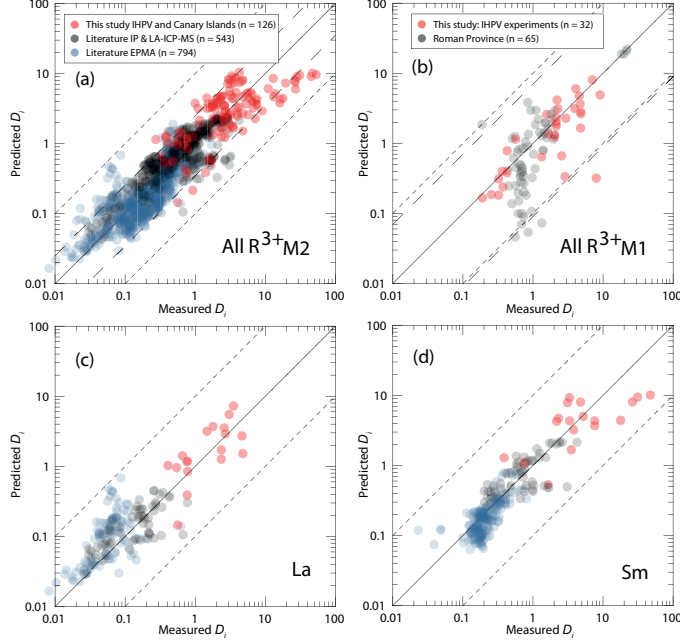


Figure 13: Measured clinopyroxene–silicate melt partition coefficients for 3+ cations vs. those predicted by our empirical model. (a) shows a comparison between measured partition coefficients and model-derived values for the $VIII\text{M}2$ site of clinopyroxene. Hard dashed lines represent 95% confidence intervals of the model, and correspond to maximum uncertainties of factor $\frac{+2.5}{-2.9}$. Fine dashed lines represent 1 order of magnitude uncertainty (extreme outliers for $VIII\text{M}2$ model). Partition coefficients in this diagram are the REE La to Er for our IHPV experiments, Canary Islands rocks, and literature data from the Italian volcanoes (Wood and Trigila, 2001; Fedele et al., 2009; Mollo et al., 2013, 2016), and all the REE plus Y for the rest of the data compilation (Bédard, 2014), which is split by analytical methodology. (b) shows performance of the predictive model for the $VI\text{M}1$ site that is calibrated for alkaline magmatic systems, and includes data from our IHPV experiments and the Italian volcanoes (Fedele et al., 2009; Mollo et al., 2013, 2016). Maximum uncertainties at the 95% confidence interval are a factor of $\frac{+7}{-11}$, higher than for the $VIII\text{M}2$ site because of the smaller calibrating data set. (c) performance of the $VIII\text{M}2$ site model for La, and (d) for Sm.

701 small relative to that for the ^{VIII}M2 site ($n = 18$), and because it is strongly
 702 skewed toward alkaline compositions, it has lower predictive power and is
 703 not recommended for application to mafic magmatic systems. Equations for
 704 the ^{VI}M1 site lattice-strain parameters, as generated by multiple linear least
 705 squares regression, are given below and shown in Figure 12 where b_i are the
 706 regression coefficients (Table 5) for the respective variables:

$$\ln D_0^{M1} = b_1 + b_2 X_{Al}^T + b_3 X_{Fe^{3+}}^{M1} + b_4 X_{Ca}^{M2} + b_5 X_{Na}^{M2} \quad (9)$$

$$E^{M1} = b_6 + b_7 T + b_8 P + b_9 X_{Mg}^{M1} \quad (10)$$

$$r_0^{M1} = b_{10} + b_{11} P + b_{12} X_{Mg}^{M2} + b_{13} X_{Fe^{3+}}^{M1} + b_{14} X_{Ca}^{M2} \quad (11)$$

707 The model for r_0^{M1} is robust and accurately reproduces the input data
 708 set. A negative pressure term may reflect compressional strain on the crystal
 709 lattice. Fe³⁺ cations have a positive effect on the size of the ^{VI}M1 site, while
 710 smaller Mg²⁺ cations on the neighbouring ^{VIII}M2 site have a negative effect
 711 on ^{VI}M1 site size. The small negative X_{Ca}^{M2} term is indirectly related to the
 712 size of the ^{VI}M1 site.

713 E^{M1} is predicted more accurately than E^{M2} and is largely described by
 714 variations in temperature and pressure. Much like the ^{VIII}M2 site, the stiff-
 715 ness of the ^{VI}M1 site appears to be controlled dominantly by physicochemical
 716 factors that are not recorded in the composition of the clinopyroxene.

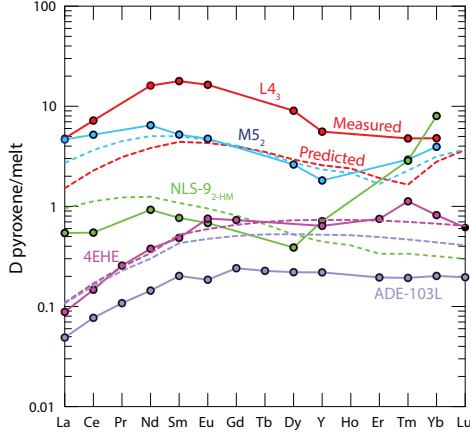


Figure 14: Measured and predicted element-partition coefficients for REE^{3+} . The model does not introduce notable radius-dependent biases, except for in our high-aegirine clinopyroxene (NLS-9_{2-HM} in green) for which D_{HREE} are strongly underpredicted, owing to inaccurate return of D_0^{M1} . Shown for comparison are two diopside–melt pairs: 4EHE from Hill et al. (2000), grown from a synthetic (NCMAS) basaltic andesite composition and ADE-103L from Lofgren et al. (2006) grown from a picritic composition based on the Angra dos Reis meteorite.

The model for D_0^{M1} contains compositional terms from all three crystallographic sites in clinopyroxene. X_{Al}^T has a strong positive correlation with D_0^{M1} , consistent with a charge compensation mechanism that aids incorporation of R^{3+} cations, while terms for ^{VI}M1 and ^{VIII}M2 site cations may be indirectly recording melt compositional effects. Because D_0^{M1} is unusually high for our high-aegirine experiments, they had to be excluded from the fitting procedure to permit model convergence. Therefore while the models for r_0^{M1} and E^{M1} are calibrated for use all the way to end-member aegirine the model for the D_0^{M1} term is only calibrated for use up to $\sim\text{Ae}_{50}$. Further experiments at conditions between those that generated our medium

727 and high-aegirine clinopyroxene would be required to better constrain the
728 clinopyroxene compositional record of D_0^{M1} in strongly peralkaline Fe-rich
729 magmas.

730 When applied to our experimental data, and the compilation of partition
731 coefficients from Italian volcanoes (Fedele et al., 2009; Mollo et al., 2013,
732 2016), the $^{VI}M1$ stepwise model reproduces element-partitioning data to a
733 factor of $\frac{+7}{-11}$ at the 95% confidence interval (Fig. 13b). Full regression
734 reports are provided in Appendix E.

735 For convenience we provide an EXCEL spreadsheet for calculation of
736 clinopyroxene-melt element-partition coefficients for any trace-element of 3+
737 valence that is large enough to fit onto the $^{VI}M1$ or $^{VIII}M2$ sites of clinopy-
738 roxene (Appendix F). To assess the utility of the partitioning models and
739 to monitor for potential introduction of radius-dependent bias, we show pre-
740 dicted REE patterns normalised to measured ratios for some literature data
741 and our internally heated pressure vessel experiments (Fig. 14). The model
742 accurately reproduces REE patterns at all compositions, except for HREE
743 on the $^{VI}M1$ site of clinopyroxene at aegirine contents exceeding ~ 50 mol %
744 (NLS experiments).

745 *5.7. Implications for formation of REE deposits in evolved alkaline intrusions*

746 The solubility of REE and HFSE minerals is strongly enhanced in peral-
747 kaline melts (Watson, 1979; Linnen and Keppler, 1997; Boehnke et al., 2013;
748 Aseri et al., 2015), thus the high concentration of these elements in peralka-
749 line systems may (partially) reflect this fact (Dostal, 2017). Melts containing
750 high concentrations of REE and HFSE are thought to be generated through
751 low degrees of partial melting in the mantle, followed by residual enrichment

752 during protracted fractional crystallisation (Marks and Markl, 2017). The
753 budget of REE and HFSE in a fractionating magma is influenced by the
754 mineralogy of the crystallising assemblage, and the extent to which these
755 elements are incorporated at minor or trace concentrations.

756 Clinopyroxene is a major ferromagnesian phase that is commonly satu-
757 rated throughout the entire differentiation histories of peralkaline magmatic
758 systems (Ablay et al., 1998; Marks and Markl, 2001; Möller and Williams-
759 Jones, 2016). The composition of the fractionating clinopyroxene has a major
760 impact on the absolute REE concentrations and REE pattern of the residual
761 melt, and ultimately on the ability of a system to develop economic con-
762 centrations of the REE (Fig. 15, e.g. Kogarko, 1990; Sørensen, 1992; Marks
763 et al., 2011). Clinopyroxene in alkaline magmatic systems is initially cal-
764 cic for mafic melts, and becomes increasingly sodic as crystal fractionation
765 proceeds (Marks et al., 2004). Although the REE are compatible in the
766 majority of our experimentally generated clinopyroxene, those approaching
767 aegirine end-member composition, as found in evolved alkaline magmatic
768 systems have the lowest D_{REE} values (Fig. 6). Strongly alkaline magmatic
769 systems are thought to crystallise abundant Ca-pyroxene early in their evolu-
770 tion which may deplete residual liquids with respect to REEs. Consequently,
771 even though crystallisation of Na-pyroxene could enrich residual liquids with
772 REE, the resultant concentration of these metals in the melt would remain
773 low. However, clinopyroxene is not the only phase to crystallise from alkaline
774 magmas, and the majority of additional silicate phases, such as olivine, bi-
775 otite and feldspar have $D_{REE} << 1$, typically 1-4 orders of magnitude lower
776 than clinopyroxene (Larsen, 1979; Kovalenko et al., 1988; Mahood and Sti-

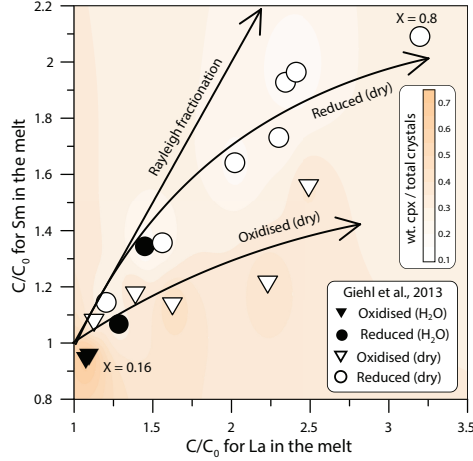


Figure 15: Model enrichment paths for La and Sm in residual melts during fractional crystallisation of a MiKa dyke composition (Gardar Province, Greenland, see Marks and Markl 2003). Phase relations and clinopyroxene compositions are from Giehl et al. (2013) and pertain to both oxidising and reducing conditions ($\log f\text{O}_2 = \Delta\text{QFM} - 3$ and +1), nominally dry to water bearing (to 3 wt.% H_2O at 1 kbar). Colour shading indicates the weight fraction of clinopyroxene within the crystallising assemblage. Bold arrows indicate residual enrichment pathways for the REE in the melt for Rayleigh fractionation (no incorporation into crystals), reduced, dry conditions, and oxidised dry conditions (the latter two are hand drawn fits to the data). For simplicity, this model does not consider REE incorporation into magnetite, alkali-feldspar, olivine, nepheline or aenigmatite, all phases generated in the experiments of Giehl et al. (2013) (see Larsen, 1979; Kovalenko et al., 1988; Mahood and Stimac, 1990).

mac, 1990; Fedele et al., 2015). Consequently, if the mode of clinopyroxene is low enough, the bulk D_{REE} of the crystallising assemblage would remain below unity, allowing the REE to become enriched in the residual silicate melt.

To give insight into the optimum conditions for residual magmatic en-

782 enrichment of the REE in alkaline systems we modelled the evolution of REE
783 concentrations in the melt during fractional crystallisation of a nepheline
784 syenite body (Fig. 15). Phase relation data and clinopyroxene compositions
785 are from the experimental study of Giehl et al. (2013). Their starting com-
786 position, based on the MiKa dyke, from the Gardar Province, Greenland, is
787 already extremely evolved, with $Mg\# = 2$, $(Na + K)/Al = 1.44$ and $FeO^* = 12$ wt.%.

788 In these models, crystallisation under water-bearing, oxidising conditions
789 produces a high fraction of clinopyroxene that depletes residual melts with
790 respect to Sm, while subtly enriching La. Dry conditions promote abun-
791 dant alkali feldspar (Afs) crystallisation, which effectively enriches the REE
792 content of residual melts. Under oxidising, dry conditions, the La/Sm ra-
793 tio of the residual melt increases with fractionation, because Sm is more
794 effectively incorporated into clinopyroxene. Residual enrichment is most ef-
795 fective under dry, reducing conditions because of a relatively lower fraction
796 of clinopyroxene within the crystallising assemblage. Because of this, the
797 REE enrichment path of the residual melt is close to that of ideal Rayleigh
798 fractionation. Under these reducing, dry conditions and at a temperature of
799 750°C, the experiments of Giehl et al. (2013) attained a crystal fraction of
800 0.8. Here, residual melts would have and 3.2 times La concentration and 2
801 times the Sm concentration relative to their starting composition.

802 Considering these mechanisms, alongside our experimental and Canary
803 Islands data, the best systems to develop high REE concentrations are those
804 that would produce small proportions of Ca-pyroxene early in their crystalli-
805 sation histories, quickly evolving to more sodic compositions that crystallise

807 aegirine clinopyroxene. Cooling under low-pressure, dry, reducing conditions
808 produces abundant alkali feldspar that in the case of a peralkaline compo-
809 sition, would serve to further increase the alkalinity of the residual melt.
810 Low-degrees of source melting would produce primary melts with (1) high
811 REE concentrations and (2) low melt Mg + Fe, and low modal abundance
812 of clinopyroxene, which would aid enrichment in residual melts via fractional
813 crystallisation.

814 The HREE-rich nature of peralkaline magmatic systems, both granites
815 and nepheline syenites, is compatible with fractionation of moderately sodic
816 clinopyroxene that have high D_{LREE}/D_{HREE} (e.g. Möller and Williams-
817 Jones, 2016; Dostal, 2017). As crystal fractionation progresses and clinopy-
818 roxene compositions evolve toward the aegirine end-member composition,
819 D_{LREE}/D_{HREE} decreases (Fig. 6). This systematic change in element-
820 partitioning behaviour would result in strong HREE enrichment in aegirine-
821 pyroxene cumulates, and would enrich the residual melt with respect to
822 LREE-MREE.

823 Conclusions

- 824 • Our experiments reveal three distinct element-partitioning behaviours
825 for Na-rich clinopyroxene that depend on aegirine content. Each of
826 these is associated with a distinct major-element exchange vector. We
827 do not have the compositional resolution to know if the transition be-
828 tween these behaviours is smooth or step-like.
- 829 • Fits to the lattice-strain model of Blundy and Wood (1994) indicate
830 expansion of the $V^{III}M_2$ site with increasing Na_{M2}^+ , to a maximum $r_{0,M2}^{3+}$

831 of 1.12 \AA at $\text{Na}_{\text{M}2}^+ = 0.4$ c.f.u. Further expansion did not occur at
832 higher Na contents.

- 833 • Both the ${}^{\text{VI}}\text{M1}$ and ${}^{\text{VIII}}\text{M2}$ sites of clinopyroxene shrink at high-aegirine
834 contents in response to increasing $\sum \text{R}_{\text{M}1}^{3+}$.
- 835 • Charge effects lead to a progressive increase in D_0^{M1} at the expense
836 of D_0^{M2} , as the exchanges Ca^{2+} for Na^+ and M^{2+} for Fe^{3+} take place.
837 Much like in systems of lower alkalinity, REE incorporation into clinopy-
838 roxene is dominated by coupled Al–Si substitutions at the ${}^{\text{IV}}\text{T}$ site.
- 839 • Existing predictive models for clinopyroxene/melt element-partitioning
840 do not accurately reproduce the large ${}^{\text{VIII}}\text{M2}$ site ($r_{0,\text{M}2}^{3+}$) of our Na-rich
841 clinopyroxene. We have calibrated a new empirical model that may be
842 applied to any composition between basalt and peralkaline phonolite,
843 based on our data from experiments and natural systems, as well as a
844 large compilation of partition coefficients from the literature.
- 845 • Crystallisation of abundant Ca-Mg rich clinopyroxene depletes the resid-
846 ual melts of REE, and inhibits or terminates orthomagmatic enrich-
847 ment processes.
- 848 • Clinopyroxene–melt REE partitioning systematics suggest that nepheline
849 syenites which host REE deposits must originate from low-degree melts
850 with sufficient alkali enrichment to saturate clinopyroxene similar to
851 our medium-aegirine clinopyroxene (Ae_{25-50}). Fractionation of such
852 clinopyroxene enriches residual melts with respect to the HREE, in

853 accord with the composition of REE-mineralised nepheline syenite sys-
854 tems.

855 **Acknowledgements**

856 We thank the Geo.X partners GFZ and Universität Potsdam for access
857 to the HP-GeoMatS Lab, Don Baker for assistance with preparation of start-
858 ing materials, Bruce Watson and Volker Möller for providing samples of Mud
859 Tank zircon and the Nechalacho Layered Suite rocks, respectively, Hans Peter
860 Nabein, Maria Stuff and Julia Pohlenz for assistance with HP experimental
861 equipment, Toby Soutar for help with preparation of the Canary Islands
862 samples, Lang Shi and Glenn Poirier for assistance with electron-microprobe
863 analyses, and Anna Jung for assistance with laser ICP-MS analyses. The
864 manuscript benefited from discussions with Longbo Yang, Rebecca Paisley,
865 Stephan Kolzenburg, Shane Rooyakkers and Jean Bédard. Silvio Mollo,
866 Lorenzo Fedele and an anonymous reviewer are thanked for their insight-
867 ful feedback. Nelson Eby is thanked for editorial handling. This work was
868 funded by PhD scholarships to C.B. from Geotop, DIVEX, and the SEG
869 Canada Foundation, and operating grants to V.vH. and J.S. from the Nat-
870 ural Sciences and Engineering Research Council of Canada (grant numbers
871 RGPIN-2014-05955, RGPAS-462335-2014) and the FQRNT team research
872 project program.

873 **References**

874 Ablay, G.J., Carroll, M.R., Palmer, M.R., Martí, J., Sparks, R.S.J.,
875 1998. Basanite–phonolite lineages of the Teide–Pico Viejo volcanic

- 876 complex, Tenerife, Canary Islands. *Journal of Petrology* 39, 905–936.
877 doi:10.1093/petroj/39.5.905.
- 878 Ablay, G.J., Ernst, G.G.J., Marti, J., Sparks, R.S.J., 1995. The 2 ka sub-
879 plinian eruption of Montaña Blanca, Tenerife. *Bulletin of Volcanology* 57,
880 337–355. doi:10.1007/BF00301292.
- 881 Adam, J., Green, T., 2006. Trace element partitioning between mica- and
882 amphibole-bearing garnet lherzolite and hydrous basanitic melt: 1. Exper-
883 imental results and the investigation of controls on partitioning behaviour.
884 *Contributions to Mineralogy and Petrology* 152, 1–17. doi:10.1007/s00410-
885 006-0085-4.
- 886 Akasaka, M., Onuma, K., 1980. The join $\text{CaMgSi}_2\text{O}_6$ - CaFeAlSiO_6 -
887 $\text{CaTiAl}_2\text{O}_6$ and its bearing on the Ti-rich fassaitic pyroxenes. *Contribu-*
888 *tions to Mineralogy and Petrology* 71, 301–312. doi:10.1007/BF00371672.
- 889 Albert, H., Costa, F., Martí, J., 2015. Timing of magmatic processes and
890 unrest associated with mafic historical monogenetic eruptions in Tenerife
891 Island. *Journal of Petrology* 56, 1945–1966. doi:10.1093/petrology/egv058.
- 892 Andújar, J., Scaillet, B., 2012. Experimental constraints on parameters con-
893 trolling the difference in the eruptive dynamics of phonolitic magmas: the
894 case of Tenerife (Canary Islands). *Journal of Petrology* 53, 1777–1806.
895 doi:10.1093/petrology/egs033.
- 896 Aseri, A.A., Linnen, R.L., Che, X.D., Thibault, Y., Holtz, F., 2015. Effects of
897 fluorine on the solubilities of Nb, Ta, Zr and Hf minerals in highly fluxed

- 898 water-saturated haplogranitic melts. *Ore Geology Reviews* 64, 736–746.
899 doi:10.1016/j.oregeorev.2014.02.014.
- 900 Beard, C.D., 2018. Mineral-melt trace element partitioning in alkaline mag-
901 matic systems. Ph.d. thesis. McGill University, Montreal, Canada.
- 902 Bédard, J.H., 2014. Parameterizations of calcic clinopyroxene - Melt trace
903 element partition coefficients. *Geochemistry, Geophysics, Geosystems* 15,
904 303–336. doi:10.1002/2013GC005112.
- 905 Behrens, H., Hahn, M., 2009. Trace element diffusion and viscous flow in
906 potassium-rich trachytic and phonolitic melts. *Chemical Geology* 259, 63–
907 77. doi:10.1016/j.chemgeo.2008.10.014.
- 908 Berndt, J., Liebske, C., Holtz, F., Freise, M., Nowak, M., Ziegenbein,
909 D., Hurkuck, W., Koepke, J., 2002. A combined rapid-quench and H₂-
910 membrane setup for internally heated pressure vessels: description and
911 application for water solubility in basaltic melts. *American Mineralogist*
912 87, 1717–1726. doi:10.1029/JB089iB10p08540.
- 913 Blundy, J., Wood, B., 1994. Prediction of crystal–melt partition coefficients
914 from elastic moduli. *Nature* 372, 452–454. doi:10.1038/372452a0.
- 915 Blundy, J.D., Robinson, J.A.C., Wood, B.J., 1998. Heavy REE are compat-
916 ible in clinopyroxene on the spinel lherzolite solidus. *Earth and Planetary
917 Science Letters* 160, 493–504. doi:10.1016/S0012-821X(98)00106-X.
- 918 Boehnke, P., Watson, E.B., Trail, D., Harrison, T.M., Schmitt, A.K.,
919 2013. Zircon saturation re-revisited. *Chemical Geology* 351, 324–334.
920 doi:10.1016/j.chemgeo.2013.05.028.

- 921 Borchert, M., Wilke, M., Schmidt, C., Cauzid, J., Tucoulou, R., 2010. Partitioning of Ba, La, Yb and Y between haplogranitic melts and aqueous solutions: An experimental study. *Chemical Geology* 276, 225–240.
922
923
924 doi:10.1016/j.chemgeo.2010.06.009.
- 925 Boudreau, A.E., 2004. PALLADIUM, a program to model the chromatographic separation of the platinum-group elements, base metals and sulfur in a solidifying pile of igneous crystals. *Canadian Mineralogist* 42, 393–403.
926
927
928 doi:10.2113/gscanmin.42.2.393.
- 929 Brown, R.J., Barry, T.L., Branney, M.J., Pringle, M.S., Bryan, S.E., 2003. The Quaternary pyroclastic succession of southeast Tenerife, Canary Islands: explosive eruptions, related caldera subsidence, and sector collapse. *Geological Magazine* 140, 265–288. doi:10.1017/S0016756802007252.
930
931
932
- 933 Bryan, S.E., Martí, J., Cas, R.A.F., 1998. Stratigraphy of the Bandas del Sur Formation: an extracaldera record of Quaternary phonolitic explosive eruptions from the Las Cañadas edifice, Tenerife (Canary Islands). *Geological Magazine* 135, 605–636. doi:null.
934
935
936
- 937 Carracedo, J.C., Badiola, E.R., Guillou, H., Paterne, M., Scaillet, S., Torrado, F.J.P., Paris, R., Fra-Paleo, U., Hansen, A., 2007. Eruptive and structural history of Teide Volcano and rift zones of Tenerife, Canary Islands. *Geological Society of America Bulletin* 119, 1027–1051.
938
939
940
941 doi:10.1130/B26087.1.
- 942 Carroll, M.R., Blank, J.G., 1997. The solubility of H₂O in phonolitic melts. *American Mineralogist* 82, 549–556. doi:10.1093/petrology/32.5.1021.
943

- 944 Cherniak, D.J., Dimanov, A., 2010. Diffusion in pyroxene, mica and
945 amphibole. *Reviews in Mineralogy and Geochemistry* 72, 641–690.
946 doi:10.2138/rmg.2010.72.14.
- 947 Chou, I.M., 1986. Permeability of precious metals to hydrogen at 2 kb total
948 pressure and elevated temperatures. *American Journal of Science* 286,
949 638–658.
- 950 Corgne, A., Wood, B.J., 2005. Trace element partitioning and substitu-
951 tion mechanisms in calcium perovskites. *Contributions to Mineralogy and*
952 *Petrology* 149, 85–97. doi:10.1007/s00410-004-0638-3.
- 953 Costa, F., Chakraborty, S., Dohmen, R., 2003. Diffusion coupling between
954 major and trace elements and a model for the calculation of magma cham-
955 ber residence times using plagioclase. *Geochimica et Cosmochimica Acta*
956 67, 2189–2200. doi:10.1016/S0016-7037(00)01345-5.
- 957 Coumans, J.P., Stix, J., Clague, D.A., Minarik, W.G., Layne, G.D., 2016.
958 Melt-rock interaction near the Moho: Evidence from crystal cargo in lavas
959 from near-ridge seamounts. *Geochimica et Cosmochimica Acta* 191, 139–
960 164. doi:10.1016/j.gca.2016.07.017.
- 961 Deer, W.A., Howie, R.A., Zussman, J., 1992. An introduction to the rock-
962 forming minerals. Longman Group Ltd, New York.
- 963 Dostal, J., 2017. Rare earth element deposits of alkaline igneous rocks. *Re-*
964 *sources* 6, 1–12. doi:10.3390/resources6030034.
- 965 Downes, H., Balaganskaya, E., Beard, A., Liferovich, R., Demaiffe, D.,
966 2005. Petrogenetic processes in the ultramafic, alkaline and carbonatitic

- 967 magmatism in the Kola Alkaline Province: A review. *Lithos* 85, 48–75.
968 doi:10.1016/j.lithos.2005.03.020.
- 969 Droop, G.T.R., 1987. A general equation for estimating Fe³⁺ concentrations
970 in ferromagnesian silicates and oxides from microprobe analyses, using
971 stoichiometric criteria. *Mineralogical magazine* 51, 431–435.
- 972 Dygert, N., Liang, Y., Sun, C., Hess, P., 2014. An experimental study of
973 trace element partitioning between augite and Fe-rich basalts. *Geochimica
974 et Cosmochimica Acta* 132, 170–186. doi:10.1016/j.gca.2014.01.042.
- 975 Edgar, C.J., Wolff, J.A., Olin, P.H., Nichols, H.J., Pittari, A., Cas, R.A.F.,
976 Reiners, P.W., Spell, T.L., Martí, J., 2007. The late Quaternary Diego Her-
977 nandez Formation, Tenerife: Volcanology of a complex cycle of voluminous
978 explosive phonolitic eruptions. *Journal of Volcanology and Geothermal Re-
979 search* 160, 59–85. doi:10.1016/j.jvolgeores.2006.06.001.
- 980 Eugster, H.P., Wones, D.R., 1962. Stability relations of the ferruginous bi-
981 otite, annite. *Journal of Petrology* 3, 82–125. doi:10.1093/petrology/3.1.82.
- 982 Fedele, L., Lustrino, M., Melluso, L., Morra, V., Zanetti, A., Van-
983 nucci, R., 2015. Trace-element partitioning between plagioclase, alkali
984 feldspar, Ti-magnetite, biotite, apatite, and evolved potassic liquids from
985 Campi Flegrei (Southern Italy). *American Mineralogist* 100, 233–249.
986 doi:10.2138/am-2015-4995.
- 987 Fedele, L., Zanetti, A., Morra, V., Lustrino, M., Melluso, L., Vannucci,
988 R., 2009. Clinopyroxene/liquid trace element partitioning in natural

- 989 trachyte–trachyphonolite systems: insights from Campi Flegrei (south-
990 ern Italy). Contributions to Mineralogy and Petrology 158, 337–356.
991 doi:10.1007/s00410-009-0386-5.
- 992 Foley, S.F., Prelevic, D., Rehfeldt, T., Jacob, D.E., 2013. Minor and
993 trace elements in olivines as probes into early igneous and mantle
994 melting processes. Earth and Planetary Science Letters 363, 181–191.
995 doi:10.1016/j.epsl.2012.11.025.
- 996 Francis, D., Minarik, W., 2008. Aluminum-dependent trace element parti-
997 tioning in clinopyroxene. Contributions to Mineralogy and Petrology 156,
998 439–451. doi:10.1007/s00410-008-0295-z.
- 999 Gaetani, G.A., 2004. The influence of melt structure on trace element par-
1000 titioning near the peridotite solidus. Contributions to Mineralogy and
1001 Petrology 147, 511–527. doi:10.1007/s00410-004-0575-1.
- 1002 Gaetani, G.A., Grove, T.L., 1995. Partitioning of rare earth elements between
1003 clinopyroxene and silicate melt: Crystal-chemical controls. Geochimica et
1004 Cosmochimica Acta 59, 1951–1962. doi:10.1016/0016-7037(95)00119-0.
- 1005 Gaillard, F., Scaillet, B., Pichavant, M., 2002. Kinetics of iron oxidation-
1006 reduction in hydrous silicic melts. American Mineralogist 87, 829–837.
1007 doi:10.2138/am-2002-0704.
- 1008 Giehl, C., Marks, M., Nowak, M., 2013. Phase relations and liquid lines
1009 of descent of an iron-rich peralkaline phonolitic melt: an experimen-
1010 tal study. Contributions to Mineralogy and Petrology 165, 283–304.
1011 doi:10.1007/s00410-012-0809-6.

- 1012 Giordano, D., Nichols, A., Dingwell, D., 2005. Glass transition temperatures
1013 of natural hydrous melts: a relationship with shear viscosity and impli-
1014 cations for the welding process. *Journal of Volcanology and Geothermal*
1015 *Research* 142, 105–118. doi:10.1016/j.jvolgeores.2004.10.015.
- 1016 Girnis, A.V., Bulatov, V.K., Brey, G.P., Gerdes, A., Höfer, H.E., 2013. Trace
1017 element partitioning between mantle minerals and silico-carbonate melts
1018 at 6–12 GPa and applications to mantle metasomatism and kimberlite
1019 genesis. *Lithos* 160-161, 183–200. doi:10.1016/j.lithos.2012.11.027.
- 1020 Goodenough, K.M., Schilling, J., Jonsson, E., Kalvig, P., Charles, N., Tuduri,
1021 J., Deady, E.A., Sadeghi, M., Schiellerup, H., Müller, A., Bertrand, G.,
1022 Arvanitidis, N., Eliopoulos, D.G., Shaw, R.A., Thrane, K., Keulen, N.,
1023 2016. Europe's rare earth element resource potential: An overview of
1024 REE metallogenetic provinces and their geodynamic setting. *Ore Geology
1025 Reviews* 72, 838–856. doi:10.1016/j.oregeorev.2015.09.019.
- 1026 Grove, T.L., Baker, M.B., Kinzler, R.J., 1984. Coupled CaAl-NaSi dif-
1027 fusion in plagioclase feldspar: Experiments and applications to cooling
1028 rate speedometry. *Geochimica et Cosmochimica Acta* 48, 2113–2121.
1029 doi:10.1016/0016-7037(84)90391-0.
- 1030 Guillou, H., Carracedo, J.C., Paris, R., Pérèz Torrado, F.J., 2004. Implica-
1031 tions for the early shield-stage evolution of Tenerife from K/Ar ages and
1032 magnetic stratigraphy. *Earth and Planetary Science Letters* 222, 599–614.
1033 doi:10.1016/j.epsl.2004.03.012.
- 1034 Gurenko, A.A., Hoernle, K.A., Hauff, F., Schmincke, H.U., Han, D., Miura,

- 1035 Y.N., Kaneoka, I., 2006. Major, trace element and NdSrPbOHeAr isotope
1036 signatures of shield stage lavas from the central and western Canary Is-
1037 lands: Insights into mantle and crustal processes. *Chemical Geology* 233,
1038 75–112. doi:10.1016/j.chemgeo.2006.02.016.
- 1039 Hanchar, J.M., Finch, R.J., Hoskin, P.W.O., Watson, E.B., Cher-
1040 niak, D.J., Mariano, A.N., 2001. Rare earth elements in synthetic
1041 zircon: Part 1. Synthesis, and rare earth element and phospho-
1042 rus doping. *American Mineralogist* 86, 667–680. doi:10.1130/0091-
1043 7613(1990)018;0757:CTOGAS;2.3.CO;2.
- 1044 Hazen, R.M., Finger, L.W., 1979. Bulk modulus-volume relationship for
1045 cation-anion polyhedra. *Journal of Geophysical Research: Solid Earth* 84,
1046 6723–6728. doi:10.1029/JB084iB12p06723.
- 1047 Hill, E., Blundy, J.D., Wood, B.J., 2011. Clinopyroxene-melt trace ele-
1048 ment partitioning and the development of a predictive model for HFSE
1049 and Sc. *Contributions to Mineralogy and Petrology* 161, 423–438.
1050 doi:10.1007/s00410-010-0540-0.
- 1051 Hill, E., Wood, B.J., Blundy, J.D., 2000. The effect of Ca-Tschermaaks com-
1052 ponent on trace element partitioning between clinopyroxene and silicate
1053 melt. *Lithos* 53, 203–215. doi:10.1016/S0024-4937(00)00025-6.
- 1054 Huang, F., Lundstrom, C.C., McDonough, W.F., 2006. Effect of melt
1055 structure on trace-element partitioning between clinopyroxene and sili-
1056 cic, alkaline, aluminous melts. *American Mineralogist* 91, 1385–1400.
1057 doi:10.2138/am.2006.1909.

- 1058 Jugo, P.J., Wilke, M., Botcharnikov, R.E., 2010. Sulfur K-edge XANES anal-
1059 ysis of natural and synthetic basaltic glasses: Implications for S speciation
1060 and S content as function of oxygen fugacity. *Geochimica et Cosmochimica
1061 Acta* 74, 5926–5938. doi:10.1016/j.gca.2010.07.022.
- 1062 Kennedy, A.K., Lofgren, G.E., Wasserburg, G.J., 1993. An experimental
1063 study of trace element partitioning between olivine, orthopyroxene and
1064 melt in chondrules: equilibrium values and kinetic effects. *Earth and Plan-
1065 etary Science Letters* 115, 177–195. doi:10.1016/0012-821X(93)90221-T.
- 1066 Kogarko, L.N., 1990. Ore-forming potential of alkaline magmas. *Lithos* 26,
1067 167–175. doi:10.1016/0024-4937(90)90046-4.
- 1068 Kovalenko, V.I., Hervig, R.L., Sheridan, M.F., 1988. Ion microprobe anal-
1069 yses of trace elements in anorthoclase, hedenbergite, aenigmatite, quartz,
1070 apatite and glass in pantellerite: evidence for high water contents in pan-
1071 tellerite melt. *American Mineralogist* 73, 1038–1045.
- 1072 Kress, V.C., Carmichael, I.S.E., 1991. The compressibility of silicate liquids
1073 containing Fe₂O₃ and the effect of composition, temperature, oxygen fu-
1074 gacity and pressure on their redox states. *Contributions to Mineralogy and
1075 Petrology* 108, 82–92. doi:10.1007/BF00307328.
- 1076 Kumazawa, M., 1969. The elastic constants of single-crystal or-
1077 thopyroxene. *Journal of Geophysical Research* 74, 5973–5980.
1078 doi:10.1029/JB074i025p05973.
- 1079 Larsen, L.M., 1979. Distribution of REE and other trace elements between
1080 phenocrysts and peralkaline undersaturated magmas, exemplified by rocks

- 1081 from the Gardar igneous province, south Greenland. *Lithos* 12, 303–315.
1082 doi:10.1016/0024-4937(79)90022-7.
- 1083 Law, K.M., Blundy, J.D., Wood, B.J., Ragnarsdottir, K.V., 2000. Trace ele-
1084 ment partitioning between wollastonite and silicate-carbonate melt. *Min-
1085 eralogical Magazine* 64, 651–661. doi:10.1180/002646100549670.
- 1086 Le Bas, M.J., Le Maitre, R.W., Streckeisen, A., Zanettin, B., 1986. A Chem-
1087 ical Classification of Volcanic Rocks Based on the Total Alkali-Silica Dia-
1088 gram. *Journal of Petrology* 27, 745–750. doi:10.1093/petrology/27.3.745.
- 1089 Liang, Y., Richter, F.M., Watson, E.B., 1994. Convection in multicom-
1090 ponent silicate melts driven by coupled diffusion. *Nature* 369, 390–392.
1091 doi:10.1038/369390a0.
- 1092 Linnen, R.L., Keppler, H., 1997. Columbite solubility in granitic melts:
1093 consequences for the enrichment and fractionation of Nb and Ta in the
1094 Earth's crust. *Contributions to Mineralogy and Petrology* 128, 213–227.
1095 doi:10.1007/s004100050304.
- 1096 Lofgren, G., 1989. Dynamic crystallization of chondrule melts of porphyritic
1097 olivine composition: Textures experimental and natural. *Geochimica et
1098 Cosmochimica Acta* 53, 461–470. doi:10.1016/0016-7037(89)90397-9.
- 1099 Lofgren, G.E., Huss, G.R., Wasserburg, G.J., 2006. An experimental study
1100 of trace-element partitioning between Ti-Al-clinopyroxene and melt: Equi-
1101 librium and kinetic effects including sector zoning. *American Mineralogist*
1102 91, 1596–1606. doi:10.2138/am.2006.2108.

- 1103 Lu, F., Anderson, A.T., Davis, A.M., 1995. Diffusional gradients at the crys-
1104 tal / melt interface and their effect on the compositions of melt inclusions.
1105 The Journal of Geology 103, 591–597.
- 1106 Lundstrom, C.C., Shaw, H.F., Ryerson, F.J., Phinney, D.L., Gill, J.B.,
1107 Williams, Q., 1994. Compositional controls on the partitioning of U, Th,
1108 Ba, Pb, Sr and Zr between clinopyroxene and haplobasaltic melts: impli-
1109 cations for uranium series disequilibria in basalts. Earth and Planetary
1110 Science Letters 128, 407–423. doi:10.1016/0012-821X(94)90159-7.
- 1111 Mahood, G.A., Stimac, J.A., 1990. Trace-element partitioning in pantel-
1112 lerites and trachytes. Geochimica et Cosmochimica Acta 54, 2257–2276.
1113 doi:10.1016/0016-7037(90)90050-U.
- 1114 Marks, M., Halama, R., Wenzel, T., Markl, G., 2004. Trace element vari-
1115 ations in clinopyroxene and amphibole from alkaline to peralkaline syen-
1116 ites and granites: implications for mineral-melt trace-element partitioning.
1117 Chemical Geology 211, 185–215. doi:10.1016/j.chemgeo.2004.06.032.
- 1118 Marks, M., Markl, G., 2001. Fractionation and assimilation processes in the
1119 alkaline augite syenite unit of the Ilímaussaq intrusion, south Greenland,
1120 as deduced from phase equilibria. Journal of Petrology 42, 1947–1969.
1121 doi:10.1093/petrology/42.10.1947.
- 1122 Marks, M., Markl, G., 2003. Ilímaussaq en miniature': closed-system frac-
1123 tionation in an agpaitic dyke rock from the Gardar Province, South Green-
1124 land (contribution to the mineralogy of Ilímaussaq no. 117). Mineralogical
1125 Magazine 67, 893–919. doi:10.1180/0026461036750150.

- 1126 Marks, M.A., Markl, G., 2017. A global review on agpaitic rocks. *Earth-*
1127 *Science Reviews* 173, 229–258. doi:10.1016/j.earscirev.2017.06.002.
- 1128 Marks, M.A.W., Hettmann, K., Schilling, J., Frost, B.R., Markl, G., 2011.
1129 The mineralogical diversity of alkaline igneous rocks: Critical factors for
1130 the transition from miaskitic to agpaitic phase assemblages. *Journal of*
1131 *Petrology* 52, 439–455. doi:10.1093/petrology/egq086.
- 1132 Möller, V., Williams-Jones, A.E., 2016. Petrogenesis of the Necha-
1133 lacho Layered Suite, Canada: magmatic Evolution of a REE-Nb-
1134 rich Nepheline Syenite Intrusion. *Journal of Petrology* 57, 229–276.
1135 doi:10.1093/petrology/egw003.
- 1136 Mollo, S., Blundy, J.D., Giacomoni, P., Nazzari, M., Scarlato, P., Coltorti,
1137 M., Langone, A., Andronico, D., 2017. Clinopyroxene-melt element par-
1138 titioning during interaction between trachybasaltic magma and siliceous
1139 crust: Clues from quartzite enclaves at Mt. Etna volcano. *Lithos* 284-285,
1140 447–461. doi:10.1016/j.lithos.2017.05.003.
- 1141 Mollo, S., Blundy, J.D., Iezzi, G., Scarlato, P., Langone, A., 2013. The
1142 partitioning of trace elements between clinopyroxene and trachybasaltic
1143 melt during rapid cooling and crystal growth. *Contributions to Mineralogy*
1144 and *Petrology* 166, 1633–1654. doi:10.1007/s00410-013-0946-6.
- 1145 Mollo, S., Forni, F., Bachmann, O., Blundy, J.D., De Astis, G., Scarlato,
1146 P., 2016. Trace element partitioning between clinopyroxene and trachy-
1147 phonolitic melts: A case study from the Campanian Ignimbrite (Campi
1148 Flegrei, Italy). *Lithos* 252253, 160–172. doi:10.1016/j.lithos.2016.02.024.

- 1149 Moore, G., Vennemann, T., Carmichael, I.S.E., 1998. An empirical model
1150 for the solubility of H₂O in magmas to 3 kilobars. *American Mineralogist*
1151 83, 36–42. doi:10.1016/0012-821X(73)90129-5.
- 1152 Morimoto, N., 1989. Nomenclature of pyroxenes. *Mineralogical Journal* 14,
1153 198–221. doi:10.2465/minerj.14.198.
- 1154 Mungall, J., Brenan, J., 2014. Partitioning of platinum-group elements and
1155 Au between sulfide liquid and basalt and the origins of mantle-crust frac-
1156 tionation of the chalcophile elements. *Geochimica et Cosmochimica Acta*
1157 125, 265–289. doi:10.1016/j.gca.2013.10.002.
- 1158 Mysen, B.O., Virgo, D., Seifert, F.A., 1982. The structure of silicate melts:
1159 Implications for chemical and physical properties of natural magma. *Re-
1160 views of Geophysics* 20, 353–383. doi:10.1029/RG020i003p00353.
- 1161 Mysen, B.O., Virgo, D., Seifert, F.A., 1985. Relationships between properties
1162 and structure of aluminosilicate melts. *American Mineralogist* 70, 88–105.
1163 doi:10.1007/BF00413348.
- 1164 Niu, Y., 2004. Bulk-rock major and trace element compositions of abyssal
1165 peridotites: Implications for mantle melting, melt extraction and post-
1166 melting processes beneath Mid-Ocean ridges. *Journal of Petrology* 45,
1167 2423–2458. doi:10.1093/petrology/egh068.
- 1168 Olin, P.H., Wolff, J.A., 2010. Rare earth and high field strength element par-
1169 titioning between iron-rich clinopyroxenes and felsic liquids. *Contributions*
1170 to *Mineralogy and Petrology* 160, 761–775. doi:10.1007/s00410-010-0506-2.

- 1171 Onuma, N., Higuchi, H., Wakita, H., Nagasawa, H., 1968. Trace element
1172 partition between two pyroxenes and the host lava. *Earth and Planetary*
1173 *Science Letters* 5, 47–51. doi:10.1016/S0012-821X(68)80010-X.
- 1174 Paton, C., Hellstrom, J., Paul, B., Woodhead, J., Hergt, J., 2011. Io-
1175 lite: Freeware for the visualisation and processing of mass spectromet-
1176 ric data. *Journal of Analytical Atomic Spectrometry* 26, 2508–2518.
1177 doi:10.1039/C1JA10172B.
- 1178 Peters, S.T., Troll, V.R., Weis, F.A., Dallai, L., Chadwick, J.P., Schulz, B.,
1179 2017. Amphibole megacrysts as a probe into the deep plumbing system
1180 of Merapi volcano, Central Java, Indonesia. *Contributions to Mineralogy*
1181 and Petrology 172, 1–20. doi:10.1007/s00410-017-1338-0.
- 1182 Putirka, K.D., 2008. Thermometers and Barometers for Volcanic
1183 Systems. *Reviews in Mineralogy and Geochemistry* 69, 61–120.
1184 doi:10.2138/rmg.2008.69.3.
- 1185 Rapp, R.P., Watson, E.B., 1986. Monazite solubility and dissolution ki-
1186 netics: implications for the thorium and light rare earth chemistry of
1187 felsic magmas. *Contributions to Mineralogy and Petrology* 94, 304–316.
1188 doi:10.1007/BF00371439.
- 1189 Rasband, W., 2016. ImageJ, U.S. National Institutes of Health, Bethesda,
1190 Maryland, USA.
- 1191 Redhammer, G.J., Amthauer, G., Roth, G., Tippelt, G., Lotter-
1192 moser, W., 2006. Single-crystal X-ray diffraction and temperature
1193 dependent ^{57}Fe Mössbauer spectroscopy on the hedenbergite-aegirine

- 1194 (Ca,Na)(Fe²⁺,Fe³⁺)Si₂O₆ solid solution. American Mineralogist 91,
1195 1271–1292. doi:10.2138/am.2006.2173.
- 1196 Reguir, E.P., Chakhmouradian, A.R., Pisiak, L., Halden, N.M., Yang, P.,
1197 Xu, C., Kynický, J., Couëslan, C.G., 2012. Trace-element composition
1198 and zoning in clinopyroxene- and amphibole-group minerals: Implications
1199 for element partitioning and evolution of carbonatites. Lithos 128, 27–45.
1200 doi:10.1016/j.lithos.2011.10.003.
- 1201 Rubatto, D., Hermann, J., 2007. Experimental zircon/melt and
1202 zircon/garnet trace element partitioning and implications for the
1203 geochronology of crustal rocks. Chemical Geology 241, 38–61.
1204 doi:10.1016/j.chemgeo.2007.01.027.
- 1205 Schmidt, B.C., Behrens, H., 2008. Water solubility in phonolite melts: Influ-
1206 ence of melt composition and temperature. Chemical Geology 256, 259–
1207 268. doi:10.1016/j.chemgeo.2008.06.043.
- 1208 Schmidt, K.H., Bottazzi, P., Vannucci, R., Mengel, K., 1999. Trace element
1209 partitioning between phlogopite, clinopyroxene and leucite lamproite melt.
1210 Earth and Planetary Science Letters 168, 287–299. doi:10.1016/S0012-
1211 821X(99)00056-4.
- 1212 Schmidt, M.W., Connolly, J.A.D., Günther, D., Bogaerts, M., 2006. Element
1213 partitioning: The role of melt structure and composition. Science 312,
1214 1646–1650. doi:10.1126/science.1126690.
- 1215 Severs, M.J., Beard, J.S., Fedele, L., Hanchar, J.M., Mutchler, S.R., Bodnar,
1216 R.J., 2009. Partitioning behavior of trace elements between dacitic melt

- 1217 and plagioclase, orthopyroxene, and clinopyroxene based on laser ablation
1218 ICPMS analysis of silicate melt inclusions. *Geochimica et Cosmochimica*
1219 *Acta* 73, 2123–2141. doi:10.1016/j.gca.2009.01.009.
- 1220 Shannon, R., 1976. Revised effective ionic radii and systematic studies of
1221 interatomic distances in halides and chalcogenides. *Acta Crystallographica*
1222 Section A 32, 751–767.
- 1223 Shea, T., Hammer, J.E., 2013. Kinetics of cooling- and decompression-
1224 induced crystallization in hydrous mafic-intermediate magmas.
1225 *Journal of Volcanology and Geothermal Research* 260, 127–145.
1226 doi:10.1016/j.jvolgeores.2013.04.018.
- 1227 Shearer, C.K., Larsen, L.M., 1994. Sector-zoned aegirine from the Ilimaussaq
1228 alkaline intrusion, South Greenland; implications for trace-element behav-
1229 ior in pyroxene. *American Mineralogist* 79, 340–352.
- 1230 Sjöqvist, A., Cornell, D., Andersen, T., Erambert, M., Ek, M., Leijd, M.,
1231 2013. Three compositional varieties of rare-earth element ore: Eudialyte-
1232 group minerals from the Norra Kärr alkaline complex, Southern Sweden.
1233 *Minerals* 3, 94–120. doi:10.3390/min3010094.
- 1234 Sørensen, H., 1992. Agpaitic nepheline syenites: a potential source of
1235 rare elements. *Applied Geochemistry* 7, 417–427. doi:10.1016/0883-
1236 2927(92)90003-L.
- 1237 Spera, F.J., Bohrson, W.A., 2001. Energy-constrained open-system mag-
1238 matic processes I: General model and energy-constrained assimilation and

- 1239 fractional crystallization (EC-AFC) formulation. *Journal of Petrology* 42,
1240 999–1018. doi:10.1093/petrology/42.5.999.
- 1241 Stevens, J., 1996. Applied multivariate analysis for the social sciences.
1242 Lawrence Erlbaum, Mahwah, NJ.
- 1243 Sun, C., Liang, Y., 2012. Distribution of REE between clinopyroxene and
1244 basaltic melt along a mantle adiabat: Effects of major element composi-
1245 tion, water, and temperature. *Contributions to Mineralogy and Petrology*
1246 163, 807–823. doi:10.1007/s00410-011-0700-x.
- 1247 Thirlwall, M.F., Singer, B.S., Marriner, G.F., 2000. ^{39}Ar - ^{40}Ar ages and
1248 geochemistry of the basaltic shield stage of Tenerife, Canary Islands,
1249 Spain. *Journal of Volcanology and Geothermal Research* 103, 247–297.
1250 doi:10.1016/S0377-0273(00)00227-4.
- 1251 Troll, V., Schmincke, H., 2002. Magma mixing and crustal recycling recorded
1252 in ternary feldspar from compositionally zoned peralkaline ignimbrite
1253 'A', Gran Canaria, Canary Islands. *Journal of Petrology* 43, 243–270.
1254 doi:10.1093/petrology/43.2.243.
- 1255 Van Orman, J.A., Grove, T.L., Shimizu, N., 2001. Rare earth element diffu-
1256 sion in diopside: influence of temperature, pressure, and ionic radius, and
1257 an elastic model for diffusion in silicates. *Contributions to Mineralogy and*
1258 *Petrology* 141, 687–703. doi:10.1007/s004100100269.
- 1259 Walker, D., Kirkpatrick, R.J., Longhi, J., Hays, J.F., 1976. Crystallization
1260 history of lunar picritic basalt sample 12002: Phase-equilibria and cooling-

- 1261 rate studies. *Bulletin of the Geological Society of America* 87, 646–656.
1262 doi:10.1130/0016-7606.
- 1263 Watson, E.B., 1979. Zircon saturation in felsic liquids: Experimental results
1264 and applications to trace element geochemistry. *Contributions to Miner-*
1265 *alogy and Petrology* 70, 407–419. doi:10.1007/BF00371047.
- 1266 Weidner, D.J., Vaughan, M.T., 1982. Elasticity of pyroxenes: Effects of
1267 composition versus crystal structure. *Journal of Geophysical Research* 87,
1268 9349–9353.
- 1269 Wiesmaier, S., Troll, V.R., Carracedo, J.C., Ellam, R.M., Bindeman, I.,
1270 Wolff, J.A., 2012. Bimodality of lavas in the Teide–Pico Viejo Succession
1271 in Tenerife—the role of crustal melting in the origin of recent phonolites.
1272 *Journal of Petrology* 53, 2465–2495. doi:10.1093/petrology/egs056.
- 1273 Wood, B.J., Blundy, J.D., 1997. A predictive model for rare earth
1274 element partitioning between clinopyroxene and anhydrous silicate
1275 melt. *Contributions to Mineralogy and Petrology* 129, 166–181.
1276 doi:10.1007/s004100050330.
- 1277 Wood, B.J., Blundy, J.D., 2001. The effect of cation charge on crystal–melt
1278 partitioning of trace elements. *Earth and Planetary Science Letters* 188,
1279 59–71. doi:10.1016/S0012-821X(01)00294-1.
- 1280 Wood, B.J., Blundy, J.D., 2003. Trace element partitioning under crustal
1281 and uppermost mantle conditions: The influences of ionic radius, cation
1282 charge, pressure, and temperature, in: Carlson, R.W. (Ed.), *The Mantle*

- 1283 and Core: Treatise on Geochemistry. Elsevier. volume 2. chapter 2.09, pp.
1284 395–424. doi:10.1016/B0-08-043751-6/02009-0.
- 1285 Wood, B.J., Blundy, J.D., 2014. Trace element partitioning: The influences
1286 of ionic radius, cation charge, pressure, and temperature, in: Carlson,
1287 R.W. (Ed.), The Mantle and Core: Treatise on Geochemistry: Second Edi-
1288 tion. Elsevier. chapter 3.11, pp. 421–445. doi:10.1016/B978-0-08-095975-
1289 7.00206-0.
- 1290 Wood, B.J., Trigila, R., 2001. Experimental determination of aluminous
1291 clinopyroxene–melt partition coefficients for potassic liquids, with applica-
1292 tion to the evolution of the Roman province potassic magmas. Chemical
1293 Geology 172, 213–223. doi:10.1016/S0009-2541(00)00259-X.
- 1294 Workman, R.K., Hart, S.R., 2005. Major and trace element composition of
1295 the depleted MORB mantle (DMM). Earth and Planetary Science Letters
1296 231, 53–72. doi:10.1016/j.epsl.2004.12.005.
- 1297 Wörner, G., Beusen, J.M., Duchateau, N., Gijbels, R., Schmincke, H.U.,
1298 1983. Trace element abundances and mineral/melt distribution coefficients
1299 in phonolites from the Laacher See volcano (Germany). Contributions to
1300 Mineralogy and Petrology 84, 152–173. doi:10.1007/BF00371282.
- 1301 Xu, C., Kynicky, J., Chakhmouradian, A.R., Campbell, I.H., Allen, C.M.,
1302 2010. Trace-element modeling of the magmatic evolution of rare-earth-rich
1303 carbonatite from the Miaoya deposit, Central China. Lithos 118, 145–155.
1304 doi:10.1016/j.lithos.2010.04.003.

- 1305 Yang, L., van Hinsberg, V.J., Samson, I., 2018. A new method to deconvolute
1306 binary mixture in LA-ICP-MS analyses to quantify the composition of
1307 phases smaller than the laser spot size. *Journal of Analytical Atomic*
1308 *Spectrometry* 33, 1518–1528. doi:10.1039/C8JA00078F.
- 1309 Yao, L., Sun, C., Liang, Y., 2012. A parameterized model for REE distri-
1310 bution between low-Ca pyroxene and basaltic melts with applications to
1311 REE partitioning in low-Ca pyroxene along a mantle adiabat and dur-
1312 ing pyroxenite-derived melt and peridotite interaction. *Contributions to*
1313 *Mineralogy and Petrology* 164, 261–280. doi:10.1007/s00410-012-0737-5.
- 1314 Zhang, Y., Ni, H., Chen, Y., 2010. Diffusion data in silicate melts. *Reviews*
1315 *in Mineralogy and Geochemistry* 72, 311–408. doi:10.2138/rmg.2010.72.8.

¹³¹⁶ **6. Tables**

Table 1: Major-element composition (in wt%) of starting materials for the internally heated pressure vessel experiments. The totals are calculated with all iron as FeO.

Dry starting glass compositions calculated from masses of reagents added [wt%]

Composition	SiO ₂	TiO ₂	Al ₂ O ₃	FeOT	MgO	CaO	Na ₂ O	K ₂ O	Total	(Na+K)/Al
L4	57.48	1.50	19.00	5.89	1.61	3.21	7.33	3.98	100.00	0.861
L5	61.24	0.68	19.51	3.77	0.43	0.91	8.63	4.84	100.00	0.996
M3	52.67	2.27	18.13	7.86	2.75	5.40	7.19	3.73	100.00	0.875
M4	56.35	1.47	18.63	5.77	1.58	3.15	8.48	4.57	100.00	1.014
M5	60.04	0.66	19.13	3.69	0.42	0.89	9.76	5.41	100.00	1.145
H4	54.80	1.43	18.12	5.62	1.54	3.06	10.07	5.38	100.00	1.236
H5	58.38	0.65	18.60	3.59	0.41	0.86	11.31	6.20	100.00	1.362

Water saturated glass compositions from superliquidus experiments (EPMA) [wt%]

L5	57.46	0.643	16.59	2.363	0.404	0.985	7.840	4.462	90.75	1.069
s.d. (n = 8)	0.299	0.087	0.210	0.059	0.035	0.050	0.175	0.132	0.351	0.017
rsd	0.52%	13.58%	1.26%	2.51%	8.70%	5.09%	2.23%	2.97%	0.39%	1.57%
H5	55.58	0.612	16.21	2.568	0.422	0.906	10.77	5.732	92.80	1.476
s.d. (n = 13)	0.327	0.057	0.221	0.113	0.044	0.049	0.205	0.154	0.417	0.028
rsd	0.59%	9.33%	1.36%	4.41%	10.44%	5.40%	1.90%	2.69%	0.45%	1.87%

Table 2: Summary of run conditions and run products for the internally-heated pressure vessel experiments.

Experiment	Setup	Pressure [bar]	Cooling ramp				(after ramp) [h,m]	Run products
			Rate °C /min	Cycle +10°C	TE-1/TE-3 [°C]	TE-2 (spl) [°C]		
L4 ₃	IHPV RQ (f)	2038	1	Y	825	828	44h50m	Cpx + Ox + Ttn + Melt
L5 ₃	IHPV RQ (f)	2038	1	Y	825	828	44h50m	Cpx + Ox + Melt
M3 ₂	IHPV RQ	2020	1	Y	796/795	799	47h	Cpx + Ox + Bt + Melt
M4 ₄	IHPV RQ	2020	1	Y	796/795	799	47h	Cpx + Ox + Bt + Melt
M5	IHPV	2000	-	-	800	799	47h55m	Cpx + Bt + Fsp + Melt
M5 ₂	IHPV RQ	2000	-	-	700	689	45h45m	Cpx + Bt + Fsp + Melt
H4 ₂	IHPV	2000	-	-	800	799	47h55m	Cpx + Ttn + Melt
H5 ₂	IHPV RQ	2000	-	-	700	689	45h45m	Cpx + Bt + Fsp + Melt
H5 ₃	IHPV RQ	2020	-	-	651/649	648	46h15m	Cpx + Bt + Fsp + Melt
NLS-9	IHPV RQ	2020	1	Y	651/649	648	46h15m	Cpx + Ox + Melt
NLS-9 ₂ HM	IHPV RQ**	2000	1	Y	650	655	42h	Cpx + Ox + Fsp + Melt

(f) indicates failure of the rapid quench apparatus; ** indicates use of a haematite double capsule, for run conditions at the haematite-magnetite $f\text{O}_2$ buffer (Eugster and Wones, 1962). Cpx = clinopyroxene; Ox = spinel oxide; Ttn = titanite; Bt = biotite; Fsp = sanidine feldspar.

Table 3: Representative major-element compositions of clinopyroxene and melt for the performed internally heated pressure vessel experiments and Canary Islands phenocryst–glass pairs.

<i>Pyroxene</i>	L4 ₃	M3 ₂	M5 ₂	H5 ₃	NLS-9	NLS-9 ₂ HM	16-07 LMB	17-12 M. Samara	17-14 UMB-II	21-30 PV 2 ka
SiO ₂	44.70	40.73	47.31	46.95	50.73	51.90	52.43	51.77	51.81	52.50
TiO ₂	3.07	4.57	3.17	4.47	0.10	0.10	0.80	0.78	0.74	0.75
Al ₂ O ₃	5.23	9.26	3.08	3.10	2.46	2.96	1.33	1.24	1.27	1.22
FeO	13.31	11.72	18.84	16.95	28.14	28.61	9.71	9.62	10.51	10.02
MnO	0.01	0.01	0.01	0.00	0.25	0.17	0.78	0.84	0.91	0.81
MgO	9.09	9.28	5.55	6.05	0.05	0.07	12.30	12.64	12.07	11.88
CaO	19.49	22.17	16.11	15.29	5.88	3.14	21.90	21.76	21.52	22.02
Na ₂ O	2.27	1.01	4.34	4.97	9.86	11.45	1.18	1.17	1.38	1.19
K ₂ O	0.09	0.03	0.08	0.07	0.04	0.04	0.02	0.03	0.00	0.02
Total	97.25	98.78	98.49	97.85	97.49	98.45	100.44	99.85	100.22	100.42
<i>Glass</i>										
SiO ₂	58.79	57.29	57.45	54.91	58.17	58.14	60.38	55.10	59.08	60.04
TiO ₂	0.35	0.27	0.23	0.62	0.00	0.00	0.64	1.73	0.66	0.66
Al ₂ O ₃	17.35	19.14	16.69	16.06	18.55	19.41	19.96	18.30	19.68	19.79
Fe ₂ O ₃ (T)	2.35	1.35	1.01	3.16	1.67	1.91	3.65	7.22	4.02	3.96
FeO(T)	2.12	1.22	0.91	2.84	1.50	1.72	3.28	6.49	3.62	3.56
MnO	0.02	0.00	-	0.01	0.06	0.04	0.14	0.23	0.22	0.20
MgO	0.20	0.13	0.15	0.35	0.00	0.00	0.39	1.84	0.32	0.35
CaO	0.55	0.95	0.24	0.84	0.23	0.23	0.76	4.10	0.77	0.74
Na ₂ O	7.17	7.32	9.08	8.88	11.12	9.80	9.00	7.26	9.76	9.05
K ₂ O	4.68	4.10	4.68	5.30	1.51	2.51	5.41	4.09	5.45	5.57
Total	91.23	90.41	89.43	89.81	91.15	91.85	99.95	99.13	99.56	99.95
(Na+K)/Al	0.97	0.86	1.15	1.27	1.07	0.97	1.01	1.12	1.09	1.09

Table 4: Pyroxene-melt trace-element-partition coefficients for representative experiments and a natural phenocryst-glass pair.

-	L4 ₃		M3 ₂		M5 ₂		H5 ₃		NLS-9		NLS-9 ₂ HM		16-07-px4 LMB	
	D	σ	D	σ	D	σ	D	σ	D	σ	D	σ	D	σ
Li	0.250	0.016	0.126	0.009	0.419	0.034	0.427	0.024	0.274	0.029	0.251	0.025	0.157	0.021
Ga	0.364	0.022	0.567	0.020	0.190	0.022	-	-	-	-	-	-	0.216	0.020
Rb	0.005	0.002	0.018	0.003	0.010	0.006	0.013	0.002	0.026	0.015	-	-	0.000	0.000
Sr	0.828	0.045	0.282	0.024	1.433	0.111	0.997	0.091	0.321	0.045	0.269	0.111	0.732	0.293
Y	5.577	0.302	13.784	1.949	1.814	0.236	1.102	0.060	0.482	0.048	0.713	0.070	2.183	0.232
Zr	1.699	0.082	2.537	0.222	1.361	0.089	1.164	0.083	2.102	0.196	3.895	0.482	0.434	0.047
Nb	0.126	0.085	0.889	0.258	0.554	0.280	1.688	0.196	2.382	0.294	9.642	4.015	0.0062	0.0004
Cs	0.019	0.003	0.019	0.003	0.014	0.006	0.010	0.002	-	-	0.023	0.017	0.001	0.001
Ba	0.0364	0.0087	0.0373	0.0152	0.0388	0.0261	0.0288	0.0091	-	-	-	-	0.00004	0.00004
La	4.787	0.646	2.591	0.240	4.658	0.962	3.049	0.132	0.410	0.037	0.542	0.043	0.769	0.071
Ce	7.199	0.756	6.229	0.646	5.199	1.073	3.190	0.129	0.377	0.028	0.547	0.061	1.591	0.120
Nd	16.105	1.537	28.430	4.210	6.454	1.630	3.759	0.147	0.579	0.054	0.925	0.114	2.632	0.155
Sm	17.843	1.414	47.245	7.699	5.215	1.293	3.113	0.137	0.388	0.070	0.767	0.182	3.522	0.421
Eu	16.403	1.341	53.195	8.181	4.743	1.132	2.900	0.133	0.275	0.082	0.682	0.192	3.372	0.196
Dy	9.027	0.537	27.082	3.925	2.619	0.460	1.521	0.073	0.329	0.057	0.388	0.088	2.798	0.220
Tm	4.773	0.261	9.067	0.903	2.937	0.279	1.567	0.097	1.330	0.145	2.860	0.890	1.846	0.182
Yb	4.797	0.249	7.015	0.600	3.937	0.296	2.281	0.152	2.564	0.346	8.004	3.116	1.978	0.186
Hf	2.385	0.162	3.556	0.472	1.802	0.118	1.141	0.123	2.443	0.275	3.702	0.479	0.769	0.065
Ta	0.496	0.152	2.3694	0.6244	0.6502	0.2545	1.5654	0.2337	2.1082	0.1764	3.6854	0.6561	0.0153	0.0013
Pb	0.079	0.017	0.0587	0.0152	0.1142	0.0349	0.0199	0.0130	0.0884	0.0280	0.0564	0.0536	0.0203	0.0040
Th	0.201	0.034	0.3565	0.0419	0.3172	0.0321	0.2892	0.0239	0.0798	0.0240	0.0709	0.0276	0.0040	0.0003
U	-	-	0.0512	0.0331	0.1261	0.0272	0.0196	0.0103	0.0460	0.0245	0.0834	0.0342	0.0022	0.0003

Table 5: Coefficients for prediction of lattice-strain parameters for clinopyroxene ${}^{VI}M1$ and ${}^{VIII}M2$ sites from clinopyroxene composition, temperature and pressure. Fitted vs. predicted lattice-strain parameters and partition coefficients are in Figures 12–13 and full multiple linear regression reports are available in Appendix E.

Model for $\ln D_0, {}^{VIII}M2$ site (n = 82)			Model for $\ln D_0, {}^{VI}M1$ site (n = 16)		
Parameter	Coefficient	σ	Parameter	Coefficient	σ
Intercept	4.52	0.91	Intercept	5	1
${}^{VI}M1Ti$	6.8	3	TAl	4	0.5
${}^{VI}M1Al - {}^{VI}M1Fe^{3+}$	1.6	0.6	${}^{VI}M1Fe^{2+}$	2.6	0.9
${}^{VIII}M2Fe^{2+}$	-3.8	1.3	${}^{VIII}M2Na$	-8	1
T [K]	-0.0035	0.0007	${}^{VIII}M2Ca$	-3	2
TAl + TFe $^{3+}$	2.6	0.8			
R^2		0.647			0.959

Model for $E_s, {}^{VIII}M2$ site (n = 79)			Model for $E_s, {}^{VI}M1$ site (n = 18)		
Parameter	Coefficient	σ	Parameter	Coefficient	σ
Intercept	247	44	Intercept	-2322	298
${}^{VI}M1Al$	-424	144	T [K]	3.2	0.4
${}^{VI}M1Mg$	-285	102	P [GPa]	-408	145
${}^{VI}M1Ti$	-1145	378	${}^{VI}M1Mg$	-800	212
${}^{VIII}M2Mg$	-306	115			
P [GPa]	37	12			
TAl + TFe $^{3+}$	313	102			
XMg	336	102			
R^2		0.348			0.936

Model for $r_0, {}^{VIII}M2$ site (n = 82)			Model for $r_0, {}^{VI}M1$ site (n = 16)		
Parameter	Coefficient	σ	Parameter	Coefficient	σ
Intercept	1.01	0.02	Intercept	0.79	0.03
${}^{VI}M1Ti$	0.16	0.05	P [GPa]	-0.017	0.005
${}^{VI}M1Al - {}^{VI}M1Fe^{3+}$	-0.03	0.01	${}^{VIII}M2Mg$	-0.48	0.06
${}^{VIII}M2Ca$	0.09	0.02	${}^{VI}M1Fe^{3+}$	0.14	0.03
${}^{VIII}M2Na$	0.14	0.02	${}^{VIII}M2Ca$	-0.05	0.02
T [K]	-4.46E-05	1.22E-05			
R^2		0.846			0.987

1317 7. Supplementary figures

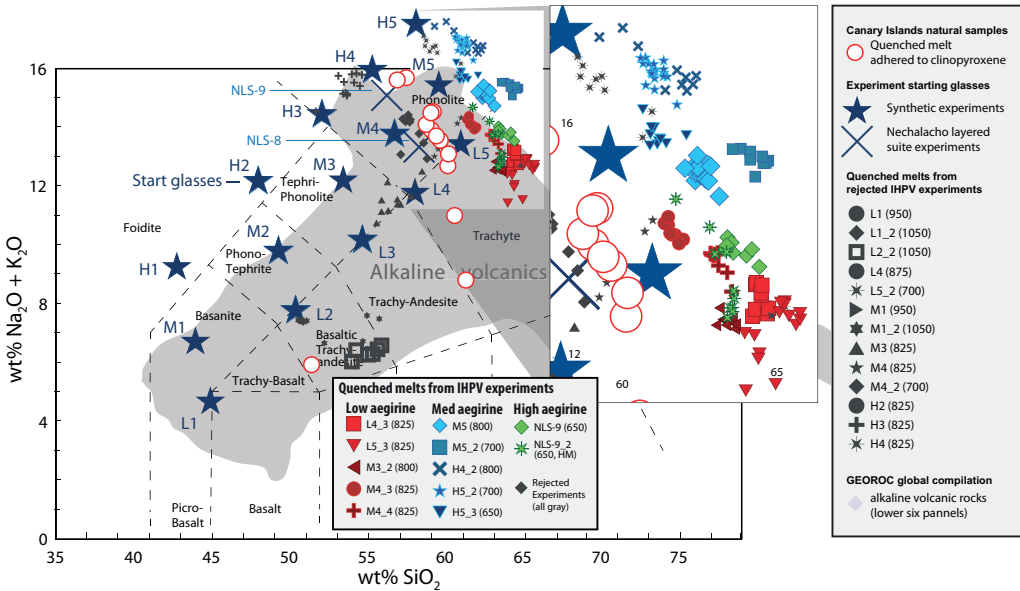


Figure S1: Total alkalies vs. silica diagram for glasses produced in internally heated pressure vessel experiments and adhered to Canary Islands clinopyroxene phenocrysts (Le Bas et al., 1986). Large stars indicate synthetic starting glass compositions as used in internally heated pressure vessel experiments (Table 1), whereas large crosses indicate the composition of powdered natural samples from the Nechalacho layered suite, NT, Canada that were used as starting materials for some experiments. The gray field indicates the compositional range expressed by alkaline volcanic provinces from around the world, sourced from the GEOROC database. Rejected experiments in dark gray are not discussed in the main text, and either did not produce clinopyroxene, produced crystals that were too small for analysis by LA-ICP-MS, or grew crystals during quench, hence preserving disequilibrium partitioning behaviour. Further diagrams showing major-element compositions for the quenched melts and the starting glasses are in Fig S2.

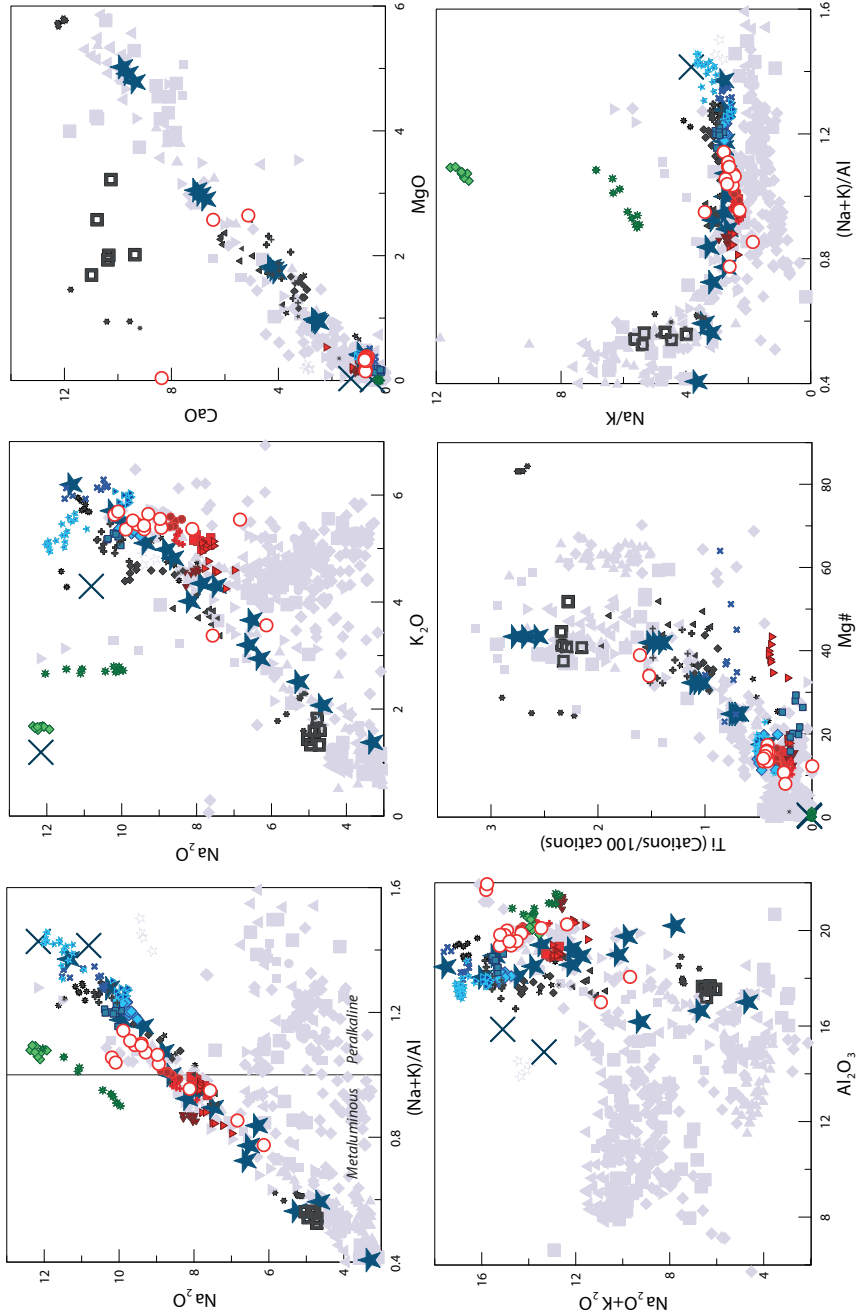


Figure S2: Major-element compositions for glass produced in the internally heated pressure vessel experiments and adhered to clinopyroxene phenocrysts from the Canary Islands. Symbols as in Fig. S1.

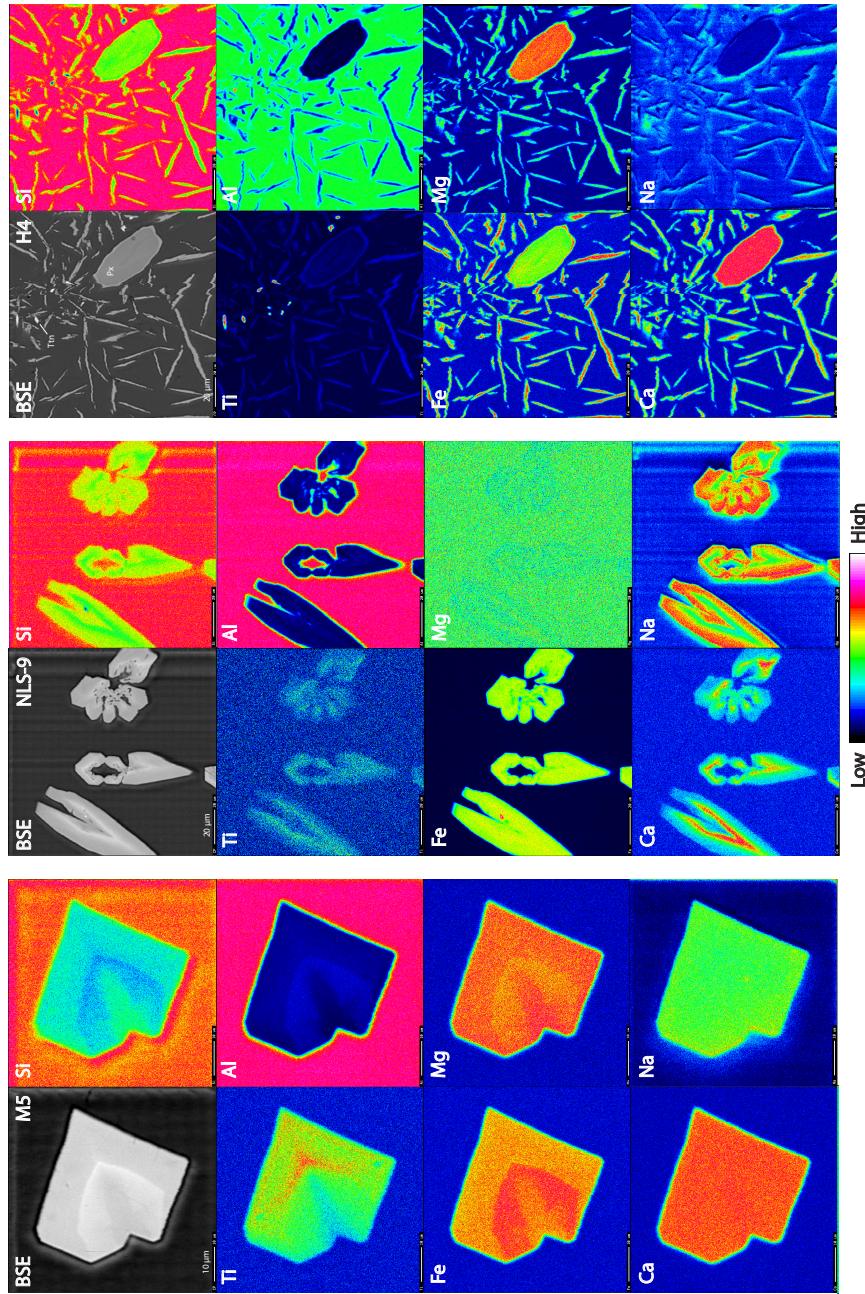


Figure S3: Element maps of clinopyroxene from internally heated pressure vessel experiments. M5 clinopyroxene have a sharp internal boundary that reflects feldspar saturation and are subtly zoned. NLS-9 clinopyroxene are more strongly zoned with swallowtail and hopper textures and rare inclusions of magnetite (cf. Walker et al., 1976; Lofgren, 1989; Shea and Hammer, 2013). H4 clinopyroxene (P_X) display a bimodal crystal size distribution and occur with titanite (Tn). The bimodal crystal size distribution is due to a temperature perturbation during run, and renders this experiment unsuitable for this element partitioning study.

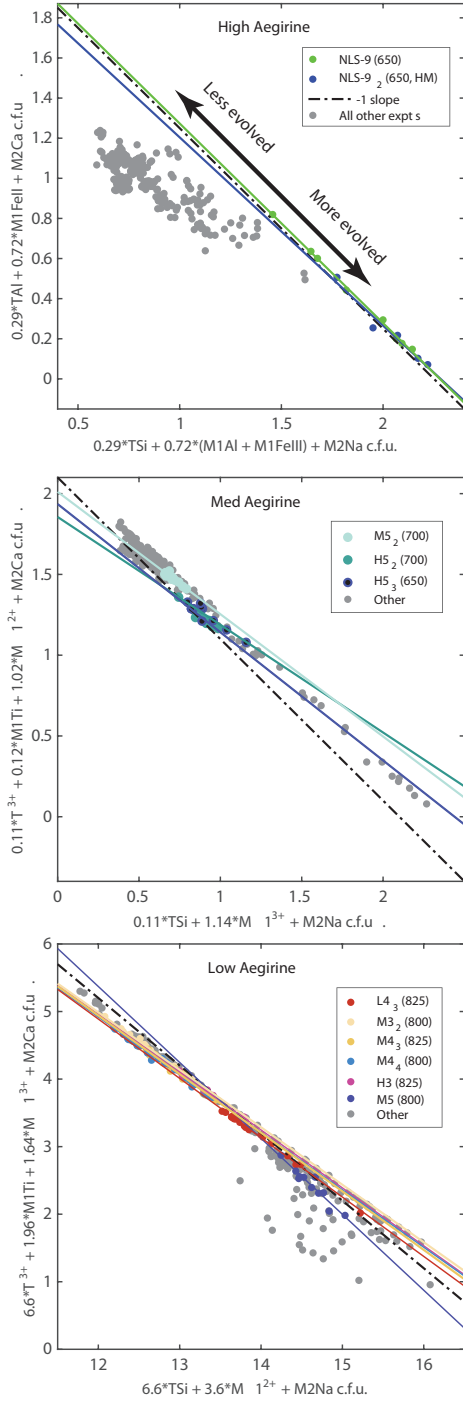


Figure S4: Major-element exchange mechanisms for (a) high, (b) medium and (c) low-aegirine clinopyroxene generated in internally heated pressure vessel experiments. Each individual plotted point represents an electron-microprobe analysis. Iron in the clinopyroxene was assigned to 2+ or 3+ valence following Droop (1987), then major-element cations were assigned to sites following Morimoto (1989, see Appendix F). Axes were defined by linear regressions between site-assigned major-element abundances, which have been checked for consistency in total site-occupancy and for charge.

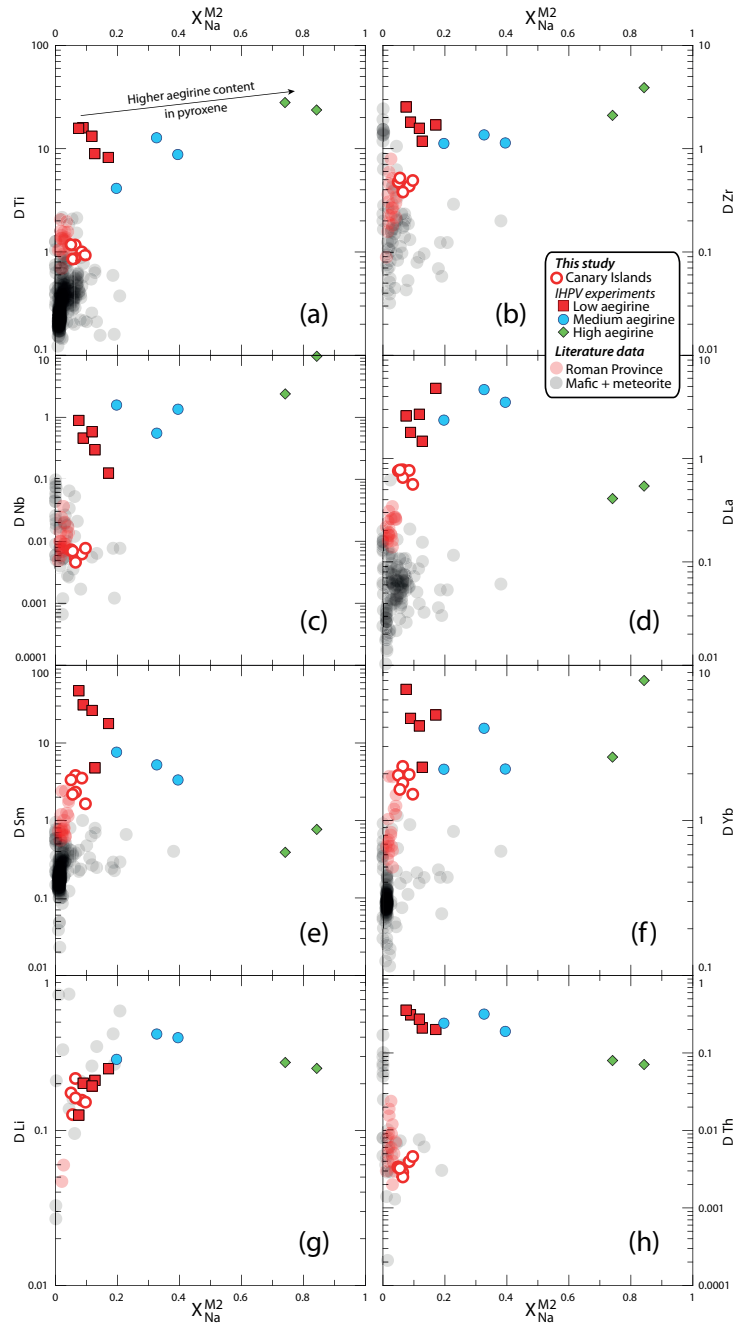


Figure S5: Element partitioning coefficients for HFSE (Ti, Zr, Nb), REE (La, Sm, Yb) and TE (Li, Th) vs. X_{Na}^{M2} . Literature values ($n = 411$), including those from Italian volcanoes, are from the compilation of Bédard (2014).

1318 **Appendix A. Electronic appendix of chemical data (.xlsx)**

1319 Electronic appendix (.xlsx file) containing experiment starting glass com-
1320 positions, experiment run conditions, mineral abundances in experimental
1321 charges, compositions of reference materials used for EPMA and LA-ICP
1322 analyses, major-element concentrations for experiment glasses and clinopy-
1323 roxene, partition coefficients and fitted lattice-strain parameters.

1324 **Appendix B. Locations for the Canary Islands samples (.kml)**

1325 Electronic appendix (.kml file) containing field locations for the Canary
1326 Islands samples.

1327 **Appendix C. The Laser Ablation ICP-MS unmixing model**

1328 The LA-ICP-MS robust regression data reduction scheme described here
1329 allows for determination of mineral trace-element compositions where the
1330 grains of interest are smaller than the laser spot-size. The mathematics
1331 underpinning the script are similar those of Rubatto and Hermann (2007)
1332 and from our research group, of Yang et al. (2018). Assumptions include...

1333 whilst effectively rejecting outlier data, for example from the ablation
1334 of minerals other than clinopyroxene that may have been hidden below the
1335 polished surfaces of the grain mounts

1336 Initially, the raw counts-per-second data are imported into Igor Pro, run-
1337 ning the iolite v2.5 extension (Paton et al., 2011) where drift and background
1338 corrections are made. Mixed signals of clinopyroxene show characteristic
1339 stepped peaks in element-ratio and beam intensity traces (Figure C.6a). Out-
1340 puts are exported in short time windows as shown.

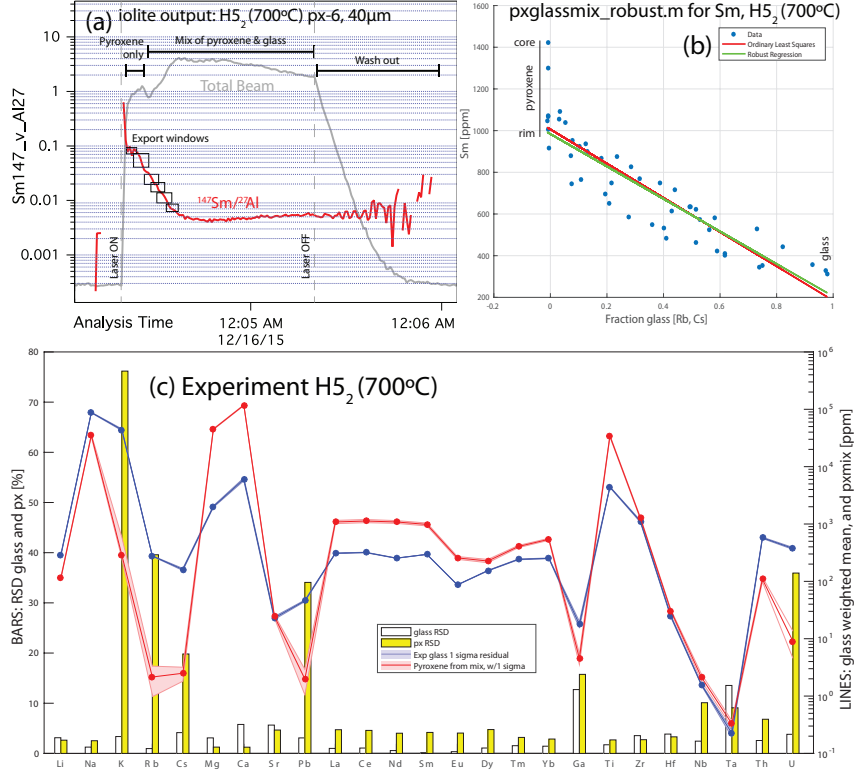


Figure C.6: An example of the robust regression data reduction scheme for laser-ablation ICP-MS analyses of glass and clinopyroxene mixtures. (a) Time series of laser-ablation data as displayed in by the iolite v2.5 extension for Igor Pro (Paton et al., 2011), (b) a MATLAB output diagram from the robust regression unmixing script, and (c) a quality control diagram output from the same MATLAB script.

1341 Trace-element concentrations in the mixes are then normalised to the sum
 1342 of major-element oxides, as measured by LA-ICP-MS.

1343 TO COMPLETE

1344 (a) Time series of laser-ablation data, showing traces for Sm/Al (red) and
 1345 total beam intensity (gray). The laser beam often ablated through the small

1346 clinopyroxene crystals, returning a mixed signal that was exported from the
1347 iolite data reduction software in short time windows as shown. Data were
1348 then normalised to the sum of major-element concentrations and mixes were
1349 deconvolved using a robust regression script written in MATLAB. (b) An
1350 example output diagram for the robust regression data reduction scheme.
1351 Clinopyroxene–glass mixing ratios were constrained by strongly incompatible
1352 elements Rb and Cs. For each element, a robust linear regression was defined
1353 between the fraction of glass in the mixture and element concentration. The
1354 intercept of this regression with zero glass returned the trace-element con-
1355 centrations in the clinopyroxene. Uncertainty with this technique is typically
1356 below 10 % relative (median 9.3 % at the 1σ level). In this example, the Sm-
1357 rich core of a zoned clinopyroxene crystal is effectively rejected during data
1358 processing, and the derived Sm concentration for the clinopyroxene is there-
1359 fore closer to that of the clinopyroxene rims that are in equilibrium with the
1360 adjacent quenched melt. (c) A quality control diagram output from the MAT-
1361 LAB data reduction scheme showing the concentrations of various elements
1362 in the glass and clinopyroxene (lines) and the uncertainty on these concen-
1363 trations expressed as a relative standard deviation (bars). Derived partition
1364 coefficients (D_i) are the mass concentration of element ‘ i ’ in clinopyroxene
1365 divided by that in the adjacent quenched melt. Residuals for the D_i values
1366 were calculated using uncertainties derived from the clinopyroxene and glass
1367 analyses to calculate minimum and maximum partition coefficients at the 1σ
1368 level. These are reported in Table 4 and Appendix A

1369 **Appendix D. EPMA Ce concentration transects across experiment**
1370 **clinopyroxene (.xlsx)**

1371 Electronic appendix (.xlsx file) containing electron-microprobe transects
1372 across experiment clinopyroxene for Ce, Mg and Fe. The data indicate that
1373 $D_{Ce}^{px/melt}$ values determined from our experiments are overestimates, but only
1374 by up to 25%. Sector zoning in the clinopyroxene appears to have a larger
1375 impact on apparent Ce partitioning behaviour than growth zoning.

1376 **Appendix E. Multiple linear regression reports (.pdf)**

1377 Electronic appendix (.pdf file) containing multiple linear regression re-
1378 ports from the stepwise fitting of 3+ cation lattice-strain parameters for the
1379 predictive model for element-partitioning (39 pages).

1380 **Appendix F. Numerical model for prediction of clinopyroxene/melt**
1381 **element-partitioning coefficients for ions of 3+ va-**
1382 **lence (.xlsx)**

1383 Electronic appendix (.xlsx file) containing a numerical model for predic-
1384 tion of clinopyroxene/melt element-partitioning coefficients for ions of 3+ va-
1385 lence. Required input data are major-element oxide compositions for clinopy-
1386 roxene, pressure and temperature. The model for the ^{VIII}M2 site is calibrated
1387 for application to systems of basaltic to peralkaline phonolite composition.
1388 The model for the ^{VI}M1 site is calibrated for use on alkaline to weakly per-
1389 alkaline systems where the aegirine mol% in clinopyroxene does not exceed
1390 50.

1391 Appendix G. Supplement: Chemical heterogeneity and the approach to equilibrium during the experiments

Appendix G.1. Attainment of equilibrium in the Canary Islands rocks

The Canary Islands trace-element partition-coefficients presented here were determined from euhedral, blade-shaped crystals free of melt inclusions and chemical zonation. The corresponding quenched melt was in direct contact with these crystals and shows no zonation in backscattered electron images (Fig. 1). While equilibrium conditions are challenging to confirm for a natural volcanic system, the euhedral forms, chemical homogeneity of crystals, and congruency between samples from separate eruptions suggest that the crystals grew in a stable environment, and were not subject to chemical or physical perturbations during growth (Fig. 6).

1403 Appendix G.2. Attainment of equilibrium in the experiments

Experiments used to determine trace-element partition-coefficients must have attained, or at least closely approached, chemical equilibrium. Unfortunately no experiments are able to determine equilibrium trace-element partition-coefficients *sensu stricto* because reversal experiments, where a clinopyroxene re-equilibrates with a melt, are not possible owing to sluggish diffusion of most elements through the clinopyroxene structure (Van Orman et al., 2001; Zhang et al., 2010). The following two sections discuss some analytical and experimental biases that must be considered when determining mineral-melt trace-element partition-coefficients from crystallisation experiments.

1414 *Appendix G.2.1. The formation of diffusive boundary layers*

1415 A potential barrier to chemical equilibration during crystallisation is the
1416 formation of a diffusive boundary layer within the melt adjacent to growing
1417 crystals. In a perfect equilibrium case there are no compositional gradients
1418 in the melt at any time during crystal growth. However in reality the growth
1419 of crystals depletes compatible elements from the melt and residually en-
1420 riches incompatible elements. Theoretically, this process of crystal growth
1421 results in formation of a (potentially ephemeral) diffusive boundary layer in
1422 the melt directly adjacent to the crystal that is depleted with respect to
1423 compatible elements and enriched with respect to those that are incompat-
1424 ible (Lu et al., 1995). The composition of such a diffusive boundary layer
1425 depends on both the relative enrichment or depletion of elements during the
1426 crystallisation process, and the rate at which these elements diffuse through
1427 the melt. Rapidly-diffusing elements with partition-coefficients close to unity
1428 will have concentrations closest to that of the bulk melt.

1429 Experiments designed to investigate trace-element-partitioning behaviour
1430 might employ slow cooling rates to limit the development of diffusive bound-
1431 ary layers, thus forming crystals from melt that is closer in composition to
1432 that of the bulk experiment. Such experiments then run into another prob-
1433 lem, in that significant crystallisation may occur at temperatures above that
1434 of the final run temperature. Rapidly-cooled experiments circumnavigate
1435 this issue, but may form relatively more pronounced diffusive boundary layers
1436 during crystal growth that become ‘flattened out’ during the homogenisation
1437 stage of the experiment.

1438 Numerous diffusion data have been gathered for silicate melts over the

1439 past few decades, and a comprehensive review is given by Zhang et al.
1440 (2010). Diffusion of trace-elements through water-saturated peralkaline melts
1441 is rapid, owing to their depolymerised structure. For example Lanthanum
1442 diffusion-coefficients are 6 orders of magnitude higher than for water-saturated
1443 granitic compositions of a similar temperature (compare Rapp and Watson,
1444 1986; Behrens and Hahn, 2009). This rapid diffusion serves to minimise the
1445 formation of diffusive boundary layers adjacent to growing crystals in our
1446 experiments. Coupled diffusion mechanisms complicate the application of
1447 measured single-element diffusion-coefficients to a crystallising system (Grove
1448 et al., 1984; Liang et al., 1994; Costa et al., 2003). Here, the diffusive flux of
1449 trace-elements may be coupled to gradients in major-element concentration
1450 within the melt.

1451 To investigate the impact of diffusive effects on trace-element-partitioning
1452 between clinopyroxene and melt, Mollo et al. (2013) performed crystallisa-
1453 tion experiments on trachybasaltic melts at a range of cooling rates (2.5–
1454 50°C / hr). Rapid cooling rates result in depletions of Si, Ca and Mg in
1455 the clinopyroxene that are compensated for by enrichments in Al, Na and
1456 Ti. Regardless of cooling rate, Ounma parabolae could be fitted through
1457 isovalent sets of partition-coefficients, indicating that crystal-lattice-effects
1458 dominated over those associated with the formation of diffusive boundary
1459 layers and that local equilibrium was achieved at the time of crystallisa-
1460 tion. In their rapidly-cooled experiments Mollo et al. (2013) found apparent
1461 clinopyroxene/melt trace-element partition-coefficients that varied with iden-
1462 tical crystal-chemical systematics to true equilibrium partition coefficients,
1463 the magnitude of both sets of trace-element partition-coefficients following

1464 the ^{IV}Al content of the clinopyroxene (ibid., their Fig. 9). Deviations of
1465 the partition coefficient of several orders of magnitude can be obtained only
1466 when rapidly growing crystals entrap small portions of the diffusive boundary
1467 layer that are found as minute melt inclusions randomly distributed in the
1468 mineral phase (Kennedy et al., 1993). In this extreme case, partitioning be-
1469 haviour is obviously influenced by contamination phenomena and no Onuma
1470 parabolae can be derived. As Onuma parabolae could successfully be fitted
1471 through partitioning data for all of our presented experiments (see following
1472 sections), and no melt inclusions were observed in optical and electron imag-
1473 ing, we infer that our data were not affected by the presence of such melt
1474 inclusions, and that they may be compared directly with partitioning data
1475 derived from experiments that employed slower cooling rates.

1476 *Appendix G.2.2. Chemical zonation in the experiment clinopyroxene: Theo-*
1477 *retical framework*

1478 Trace-elements diffuse slowly through the clinopyroxene structure relative
1479 to that of the melt (Van Orman et al., 2001; Zhang et al., 2010), therefore no
1480 re-equilibration of trace-elements takes place on an experimental time scale.
1481 Strictly speaking, clinopyroxene only record true equilibrium conditions at
1482 their outermost rim. Experiments designed for the derivation of equilibrium
1483 partition coefficients ideally minimise bias by limiting the fraction of crystalli-
1484 sation, producing minerals that are as homogeneous as possible. Currently
1485 available *in situ* analytical techniques for trace-element abundances, such as
1486 LA-ICP-MS and SIMS, are limited in terms of minimum beam-size to ~ 10
1487 μm ; chemical zonation, however subtle, will be continuous from the core to
1488 the rim of the mineral. Consequently, no experimentally-derived partition-

1489 coefficients record chemical equilibrium *sensu stricto*, but properly conducted
1490 experiments may closely approximate this state.

1491 Because only the very rim of a crystal records chemical equilibrium with
1492 the adjacent melt, and some internal portions of the minerals must be sam-
1493 pled during *in-situ* analyses all experimentally-determined trace-element partition-
1494 coefficients are biased toward higher values for compatible elements and lower
1495 values for incompatible elements. The magnitude of these biases depends
1496 on the fraction of crystallisation in the experiment, the true equilibrium
1497 partition-coefficient of that element, as well as the proportion of each growth-
1498 zone sampled during the *in-situ* analysis. Fortunately *in-situ* chemical anal-
1499 yses preferentially sample the mantle and rim of zoned crystals because few
1500 analyses section a crystal perfectly through the core. As a result there is a
1501 sampling bias toward equilibrium mineral compositions.

1502 Consider a hypothetical experimental system in which 20% of the melt
1503 crystallises as a single mineral, and where the chemical analyses of that
1504 mineral are truly bulk averages of that mineral composition. An incompatible
1505 element with a true equilibrium partition coefficient of 0.1 would return a
1506 measured partition coefficient of 0.09, a small bias because the concentration
1507 of that incompatible element in the melt changed only subtly during the
1508 course of crystallisation. For compatible elements with true D_i values of
1509 ~ 10 , measured partition coefficients can be a factor of 2–3 higher than true
1510 partition coefficients, because their concentration in the melt changes more
1511 than an incompatible element during the course of crystallisation.

1512 Further complexity is introduced in systems that crystallise multiple min-
1513 erals simultaneously. In the case of experiment M3₂, the REE are compatible

1514 in clinopyroxene, but are incompatible in biotite and oxides (e.g. Mahood and
1515 Stimac, 1990; Schmidt et al., 1999). The REE have therefore been residually
1516 enriched in the melt phase by the crystallisation of biotite and oxide miner-
1517 als, while simultaneously being depleted from the melt by crystallisation of
1518 clinopyroxene. These two competing processes serve to minimise the effect of
1519 fractional crystallisation on the concentration of trace-elements in the melt
1520 and consequently derived REE partition-coefficients between clinopyroxene
1521 and melt will be closer to true equilibrium values.

1522 *Appendix G.2.3. Implications of the cerium zonation across the experiment*
1523 *clinopyroxene*

1524 Electron-microprobe analyses offer a smaller minimum beam-size than
1525 LA-ICP-MS systems at the expense of precision and of number of elements
1526 that may be analysed simultaneously. This higher spatial resolution permit-
1527 ted investigation of the zonation of Ce concentrations within the experiment
1528 clinopyroxene, with Ce as a proxy for the other compatible elements.

1529 The magnitude of concentric growth zoning in the experiment clinopy-
1530 roxene was examined by averaging bulk and rim compositions across mul-
1531 tiple sector-zoned grains within each experiment. The median Ce counts
1532 divided by the rim Ce counts was 1.04 for experiment M3₂, 1.08 for ex-
1533 periment M5 and 1.12 for the fluorine-bearing experiment M3-1.25F (see
1534 Beard, 2018). Contrary to theory discussed above, the subtly (3%) crys-
1535 tallised experiment M5 shows a greater variation in core-to-rim Ce content
1536 than the more heavily (?? TO ADD%) crystallised experiment M3₂. Further-
1537 more, the $D_{Ce}^{cpx/melt}$ for experiment M3₂ (6.2) is approximately double that
1538 for experiment M5 (see discussion below), which should further promote the

₁₅₃₉ formation of Cerium zonation in the clinopyroxene during crystallisation.
₁₅₄₀ Consequently it is possible that many existing experimentally-derived trace-
₁₅₄₁ element partition-coefficients are systematically offset from true equilibrium
₁₅₄₂ values.

₁₅₄₃ If Cerium is used as a proxy for the behaviour of compatible elements
₁₅₄₄ in our experimental system, then apparent partition coefficients derived for
₁₅₄₅ these elements via LA-ICP-MS are systematically offset to higher values by 4–
₁₅₄₆ 8%. Such a systematic bias is small, relative to the variation in clinopyroxene-
₁₅₄₇ melt partition coefficients within our sample set, as well as in the literature.
₁₅₄₈ The effect of crystal zonation on incompatible element concentrations was
₁₅₄₉ not measured, but as outlined in the theoretical framework above, this effect
₁₅₅₀ should be smaller than that for the compatible elements. No correction factor
₁₅₅₁ has been applied to the data presented in the figures below, or in Table 4
₁₅₅₂ and Appendix A.